

High-order implicit Runge-Kutta time integrators for component-based model reduction of FSI problems

Tommaso Taddei¹, Xuejun Xu^{2,3} Lei Zhang².

¹ *Dipartimento di Matematica, Sapienza University of Rome, 00185 Rome, Italy*

`tommaso.taddei@uniroma1.it`

² *School of Mathematical Sciences, Key Laboratory of Intelligent Computing and Applications (Ministry of Education), Tongji University, Shanghai 200092, China*

`xxj@lsec.cc.ac.cn, 22210@tongji.edu.cn`

³ *Institute of Computational Mathematics, AMSS, Chinese Academy of Sciences, Beijing 100190, China*

`xxj@lsec.cc.ac.cn`

Abstract

We propose a model order reduction framework for incompressible fluid-structure interaction (FSI) problems based on high-order implicit Runge-Kutta (IRK) methods. We consider separate reduced spaces for fluid velocity, fluid pressure and solid displacement; we enrich the velocity space with supremizer modes to ensure the inf-sup stability of the fluid subproblem; we consider bubble-port decomposition of fluid velocity and solid displacement to satisfy the kinematic conditions at the fluid structure interface. We resort to Galerkin projection to define the semi-discrete reduced-order model and we consider a Radau-IIA IRK method for time integration: the resulting algebraic system is solved using static condensation of the interface degrees of freedom. The reduced-order model preserves a semi-discrete energy balance inherited from the full-order model, and avoids the need for additional interface enrichment. Numerical experiments demonstrate that the proposed combination of high-order IRK schemes with bubble-port decoupling of velocity and displacement degrees of freedom yields stable and accurate reduced-order model for long-time integration of strongly-coupled parametric FSI problems.

Keywords: model order reduction; fluid-structure interaction; implicit Runge-Kutta methods; static-condensation reduced basis element (scrBE); optimization-based coupling.

1 Introduction

1.1 Model reduction of fluid-structure interaction problems

Fluid-structure interaction (FSI) problems arise in a wide range of engineering and scientific applications, such as the aeroelastic behavior of wings and turbine blades [1, 2, 3], wave-induced dynamics of offshore structures [4, 5], hemodynamics in compliant vessels [6, 7], or micro-electro-mechanical systems (MEMS) [8, 9]. Accurate numerical simulations of coupled problems are essential for understanding, predicting, and controlling the behavior of the underlying physical system. However, despite the many recent advances, high-fidelity (HF) computational models of FSI problems are extremely computationally demanding: they are hence ill-suited to deal with real-time (e.g., control) and many-query (e.g., parametric studies, uncertainty quantification) tasks and also with long time integration.

Over the past two decades, model order reduction (MOR) [10, 11] has emerged as an effective strategy for alleviating the computational burden associated with parametric studies of engineering systems governed by partial differential equations (PDEs). By approximating the HF dynamics within a suitably chosen low-dimensional subspace, reduced-order models (ROMs) significantly lower computational demands while maintaining predictive accuracy. In particular, projection-based methods exploit (Petrov-)Galerkin projection to devise model-based ROMs of parametric systems. Traditional (monolithic) MOR methods have been successfully applied to a broad range of parametric problems, but they are ill-suited to deal with coupled and/or large-scale systems with parameter-induced topology changes for which it is not possible to define a single parameter-independent low-dimensional subspace. To address this issue, several authors have proposed component-based (CB) MOR techniques that combine traditional MOR strategies with domain decomposition (DD) methods to handle large-scale systems [12, 13, 14].

A variety of projection-based ROMs have been proposed for FSI, including monolithic POD-Galerkin approaches [15], partitioned semi-implicit schemes [16, 17], and time-segmented techniques [18]. Non-intrusive and segregated strategies have also been investigated [19, 20]. In the context of hemodynamics, Deparis and coauthors developed reduced FSI problems based on the thin-walled assumption and transpiration condition, and they applied CB-MOR techniques to further reduce the computational costs [21, 22, 14]. We refer to [23] for a

thorough overview of full-order and reduced-order methods for vascular FSI simulations; we also refer to [24] for a recent application of projection-based MOR techniques to uncertainty quantification of FSI systems in hemodynamics. Despite these advances, the development of stable and accurate ROMs for FSI remains challenging due to stringent requirements for preserving inter-domain coupling conditions and numerical stability.

A key factor that influences the stability and accuracy of FSI simulations, and thus the effectiveness of associated ROM techniques, is the choice of temporal discretization scheme. In practical FSI computations of incompressible flows, it is common to integrate the incompressible Navier–Stokes equations using the second-order backward differentiation formula (BDF2), while employing the Newmark method for structural dynamics, which results in an overall second-order accuracy in time [25, 26, 27]. However, the standard Newmark method may exhibit numerical instability for geometrically nonlinear structures, where energy transfer occurs across an infinite number of deformation modes [28, 29]. Although alternative dissipative methods, such as Bossak, generalized- α , or explicit singly diagonally implicit Runge–Kutta (ESDIRK) methods, can enhance numerical stability by effectively damping spurious high-frequency oscillations [30, 31], their inherent numerical dissipation risks to excessively attenuate physically-relevant structural dynamics.

These observations highlight the need for temporal schemes that are both strongly stable and sufficiently accurate, without relying on excessively dissipative modifications. Rather than increasing numerical damping, a more attractive strategy is to employ higher-order temporal schemes that can achieve a prescribed accuracy with larger time steps and result in superior computational efficiency, which is particularly beneficial for long-time FSI simulations [32, 33, 34, 29, 35]. However, linear multistep methods such as BDF are subject to the second Dahlquist barrier [36, 37], which prevents higher-order variants from achieving desirable stability properties such as A- and L-stability. On the other hand, fully implicit Runge–Kutta (IRK) methods [36, 38] naturally overcome these stability limitations.

In this work, we rely on Radau-IIA IRK methods for time discretization of both full-order and reduced-order models. Radau-IIA IRK methods are high-order, A-stable, L-stable, and stiffly accurate: they enable effective suppression of spurious numerical oscillations at high frequencies without compromising the accurate representation of physically relevant low-frequency dynamics [36, 37, 29]. Radau-IIA IRK methods can be applied to both fluid and structural equations and they effectively cure numerical instabilities associated with nonlinear structural dynamics encountered in Newmark-based approaches, without introducing excessive dissipation [30, 31, 39, 29].

1.2 Application of high-order implicit Runge Kutta time integrators to component-based model reduction

In this work, we aim to devise energy-stable ROMs for FSI systems: towards this end, we combine the static condensation reduced basis element (scrBE) method with the IRK time integrators discussed above. The (port-reduced) scrBE method exploits a port-bubble solution decomposition to ensure solution continuity at the interfaces (ports), and relies on static condensation to eliminate internal degrees of freedom and effectively solve the reduced system. The scrBE method was first introduced for linear coercive elliptic problems in [13] and [40] and then extended to mechanics problems with local nonlinearities in [41] and to fully-nonlinear problems in [42]. We recall that the scrBE method shares many features with component mode synthesis (CMS) in structural dynamics [43, 44, 45].

To our knowledge, the present work constitutes the first application of the scrBE method to FSI systems; we note, however, that CMS has already been applied to linearized FSI problems in [46, 47]. The combination of projection-based MOR methods with IRK time integration is also new: while the need for solving a much larger and possibly poorly-conditioned nonlinear problem has limited so far the application of IRK methods to HF FSI simulations, the additional cost at the MOR level is much less significant thanks to port reduction that enables the use of direct linear solvers.

We observe that our formulation can be interpreted as an optimization-based method where the solid displacement at the interface is treated as the control. In this respect, the method is related to previous efforts on optimization-based coupling of fluid [48] and FSI [49] problems. The methods [48, 49] (see also [50, 51]) exploit the normal flux as the control variable and were inspired by the works by Gunzburger and coauthors on optimization-based coupling of elliptic problems and the incompressible Navier–Stokes equations [52, 53] and the subsequent works on FSI [54, 55, 56]. We show that our method has two key advantages over the optimization-based coupling of [48, 49]: first, we prove a semi-discrete energy balance for the reduced system, which clearly illustrates the superior stability properties of the new formulation; second, thanks to the port-bubble decomposition the new formulation does not require any enrichment of the velocity basis to restore the full rank of the reduced Jacobian of the coupled problem.

The remainder of this paper is organized as follows. Section 2 reviews the governing equations of the FSI problem in ALE form and briefly recalls the weak formulation. Section 3 presents the finite element spatial discretization, introduces the Radau-IIA IRK time integrator, and derives the resulting fully discrete coupled system, together with the optimization-based partitioned algorithm. Section 4 presents the construction of

bubble-port reduced spaces and derives the associated semi-discrete and fully discrete ROMs. Numerical results are presented in Section 5. Section 6 provides concluding remarks and outlines future research directions.

2 Governing equations and semi-discrete formulation

We consider the interaction between an incompressible viscous fluid and an elastic solid in an Arbitrary Lagrangian Eulerian (ALE) setting. Let $\tilde{\Omega}_f, \tilde{\Omega}_s \subset \mathbb{R}^d$ ($d \in \{2, 3\}$) denote the reference fluid and solid domains, respectively, that share the interface $\tilde{\Gamma} = \partial\tilde{\Omega}_f \cap \partial\tilde{\Omega}_s$, as illustrated in Figure 1. The current fluid and solid configurations at time $t \geq 0$ are obtained through the mappings

$$\Omega_f(t) = \Phi_f(\tilde{\Omega}_f, t), \quad \Omega_s(t) = \{\tilde{\mathbf{x}} + \tilde{\mathbf{d}}_s(\tilde{\mathbf{x}}, t) : \tilde{\mathbf{x}} \in \tilde{\Omega}_s\},$$

where $\tilde{\mathbf{d}}_s$ is the solid displacement, and the current interface $\Gamma(t) = \Phi_f(\tilde{\Gamma}, t)$. The ALE velocity is $\tilde{\omega}_f = \partial_t \Phi_f$, and the ALE time derivative of any Eulerian field q is

$$\partial_t q|_{\Phi_f}(\mathbf{x}, t) := \frac{d}{dt} \left(q(\Phi_f(\tilde{\mathbf{x}}, t), t) \right), \quad \mathbf{x} = \Phi_f(\tilde{\mathbf{x}}, t). \quad (1)$$

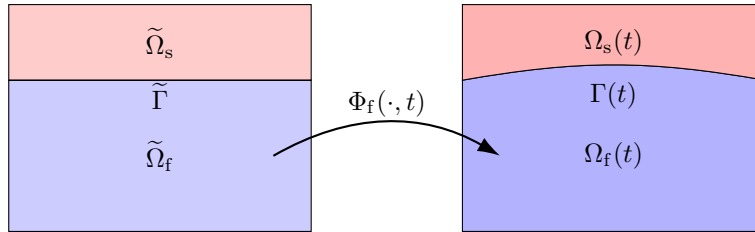


Figure 1: Reference and current domains of FSI problems. Here, $\Phi_f(t)$ is the ALE bijection that maps the reference fluid domain $\tilde{\Omega}_f$ into the current domain $\Omega_f(t)$.

We briefly recall the strong and weak formulations of the coupled FSI problem [57, 58, 59, 49].

2.1 Strong form

Fluid subproblem The fluid is governed by the incompressible Navier–Stokes in the ALE framework

$$\begin{cases} \rho_f \partial_t \mathbf{u}_f|_{\Phi_f} + \rho_f [(\mathbf{u}_f - \boldsymbol{\omega}_f) \cdot \nabla] \mathbf{u}_f - \nabla \cdot \boldsymbol{\sigma}_f = 0, & \text{in } \Omega_f(t), \\ \nabla \cdot \mathbf{u}_f = 0, & \text{in } \Omega_f(t), \\ \mathbf{u}_f|_{\Gamma^{\text{dir}}} = \mathbf{u}_f^{\text{dir}}, \quad \boldsymbol{\sigma}_f \mathbf{n}_f|_{\Gamma^{\text{neu}}} = \mathbf{g}_f^{\text{neu}}, & \end{cases} \quad (2)$$

where \mathbf{u}_f denotes the fluid velocity, ρ_f the density,

$$\boldsymbol{\sigma}_f = 2\mu_f \boldsymbol{\varepsilon}_f - p_f \mathbf{I}, \quad (\boldsymbol{\varepsilon}_f = \frac{1}{2}(\nabla \mathbf{u}_f + \nabla \mathbf{u}_f^T))$$

is the Newtonian Cauchy stress tensor, p_f is the pressure, and μ_f is the dynamic viscosity. The ALE velocity $\boldsymbol{\omega}_f$ enters in the advection term of the momentum equation to account for the fluid domain motion induced by the structural displacement.

Solid subproblem The solid is modeled by the elastodynamic equations for the displacement in the Lagrangian framework

$$\begin{cases} \tilde{\rho}_s \partial_{tt} \tilde{\mathbf{d}}_s - \tilde{\nabla} \cdot \tilde{\boldsymbol{\Pi}}_s = \mathbf{0} & \text{in } \tilde{\Omega}_s, \\ \tilde{\mathbf{d}}_s|_{\tilde{\Gamma}_s^{\text{dir}}} = \tilde{\mathbf{d}}_s^{\text{dir}}, \quad \tilde{\boldsymbol{\Pi}}_s \tilde{\mathbf{n}}_s|_{\tilde{\Gamma}_s^{\text{neu}}} = \tilde{\mathbf{g}}_s^{\text{neu}}. & \end{cases} \quad (3)$$

Here $\tilde{\rho}_s$ denotes the solid density, $\tilde{\boldsymbol{\Pi}}_s$ is the first Piola-Kirchhoff stress tensor. We consider both the small strain linear elasticity and the Saint-Venant Kirchhoff (SVK) hyperelasticity [57, pp.98-100][25, 60]. In the linear elasticity case, the first Piola-Kirchhoff stress tensor is given by

$$\tilde{\boldsymbol{\Pi}}_s = 2\mu_s \tilde{\boldsymbol{\varepsilon}}_s + \lambda_s (\tilde{\nabla} \cdot \tilde{\mathbf{d}}_s) \mathbf{I},$$

where λ_s, μ_s are the first and the second Lamé coefficients, and $\tilde{\boldsymbol{\varepsilon}}_s = \frac{1}{2}(\tilde{\nabla}\tilde{\mathbf{d}}_s + \tilde{\nabla}\tilde{\mathbf{d}}_s^\top)$ is the strain tensor in the Lagrangian frame. In the SVK case, the first Piola-Kirchhoff stress tensor is given by

$$\tilde{\boldsymbol{\Pi}}_s = \tilde{\mathbf{F}}_s \tilde{\boldsymbol{\Sigma}}_s,$$

where $\tilde{\mathbf{F}}_s = \mathbf{I} + \tilde{\nabla}\tilde{\mathbf{d}}_s$ is the deformation gradient, $\tilde{\boldsymbol{\Sigma}}_s = 2\mu_s\tilde{\mathbf{E}}_s + \lambda_s\text{tr}(\tilde{\mathbf{E}}_s)\mathbf{I}$ is the second Piola-Kirchhoff stress tensor, and $\tilde{\mathbf{E}}_s = \frac{1}{2}(\tilde{\mathbf{F}}_s^\top\tilde{\mathbf{F}}_s - \mathbf{I})$ is the Green-Lagrange tensor.

Coupling conditions On the interface $\tilde{\Gamma}$ we impose:

- (i) geometric compatibility $\Phi_f = \text{id} + \tilde{\mathbf{d}}_s$, where id is the identity map,
- (ii) kinematic continuity $\mathbf{u}_f \circ \Phi_f = \partial_t \tilde{\mathbf{d}}_s$, and
- (iii) dynamic equilibrium $\tilde{\boldsymbol{\Pi}}_s \tilde{\mathbf{n}}_s + J_\Phi(\boldsymbol{\sigma}_f \circ \Phi_f) \tilde{\nabla}\Phi_f^{-\top} \tilde{\mathbf{n}}_f = \mathbf{0}$, where $J_\Phi = \det(\tilde{\nabla}\Phi_f)$.

ALE mapping To close the system, we need to determine the ALE mapping. Following [61, 60], we define the ALE mapping Φ_f using a pseudo-elasticity model. Specifically, we define $\Phi_f = \text{id} + \tilde{\mathbf{d}}_f$, where the pseudo-displacement $\tilde{\mathbf{d}}_f$ solves a steady linear elasticity problem, with suitably-chosen pseudo material parameters. As for boundary conditions, we impose $\tilde{\mathbf{d}}_f = 0$ on $\partial\tilde{\Omega}_f \setminus \tilde{\Gamma}$, and $\tilde{\mathbf{d}}_f = \tilde{\mathbf{d}}_s$ on $\tilde{\Gamma}$ to match the solid displacement on the fluid-solid interface.

2.2 Weak formulation

We introduce the function spaces for the fluid:

$$V_f^{\text{dir}}(t) := \{\mathbf{v} \in [H^1(\Omega_f(t))]^d : \mathbf{v}|_{\Gamma_f^{\text{dir}}(t)} = \mathbf{u}_f^{\text{dir}}(t)\}, \quad V_{f,0}(t) := [H_{0,\Gamma_f^{\text{dir}}(t)}^1(\Omega_f(t))]^d, \quad Q_f(t) := L^2(\Omega_f(t)), \quad (4)$$

and for the solid

$$V_s^{\text{dir}}(t) := \{\tilde{\mathbf{v}} \in [H^1(\tilde{\Omega}_s)]^d : \tilde{\mathbf{v}}|_{\tilde{\Gamma}_s^{\text{dir}}} = \tilde{\mathbf{d}}_s^{\text{dir}}(t)\}, \quad V_{s,0} := [H_{0,\tilde{\Gamma}_s^{\text{dir}}(t)}^1(\tilde{\Omega}_s)]^d. \quad (5)$$

The weak formulation reads: For any $t > 0$, we seek $\mathbf{u}_f \in V_f^{\text{dir}}, p_f \in Q_f, \tilde{\mathbf{d}}_s \in V_s^{\text{dir}}$ such that

$$\begin{cases} \frac{d}{dt} \int_{\Omega_f(t)} \rho_f \mathbf{u}_f \cdot \mathbf{v} \, dx + R'_f(\mathbf{u}_f, p_f, \boldsymbol{\omega}_f, \mathbf{v}) + \int_{\tilde{\Omega}_s} \tilde{\rho}_s \frac{\partial^2 \tilde{\mathbf{d}}_s}{\partial t^2} \cdot \tilde{\mathbf{w}} \, dx + R'_s(\tilde{\mathbf{d}}_s, \tilde{\mathbf{w}}) = 0; \\ b_f(\mathbf{u}_f, q) = 0; \\ \Phi_f|_{\tilde{\Gamma}} = \text{id} + \tilde{\mathbf{d}}_s|_{\tilde{\Gamma}}, \quad \mathbf{u}_f \circ \Phi_f|_{\tilde{\Gamma}} = \frac{\partial \tilde{\mathbf{d}}_s}{\partial t}|_{\tilde{\Gamma}}, \end{cases} \quad (6a)$$

for any $\mathbf{v} \in V_{f,0}, \tilde{\mathbf{w}} \in V_{s,0}$ such that $\mathbf{v} \circ \Phi_f = \tilde{\mathbf{w}}$ on $\tilde{\Gamma}$ and any $q \in Q_f$. We emphasize that the test functions for the fluid and the solid velocities are chosen to match at the interface, which is consistent with the kinematic continuity condition in the strong formulation. Here, R'_f, R'_s and b_f denote the spatial parts of the fluid and solid residuals and the fluid incompressibility constraint, respectively, and are defined by

$$\begin{cases} R'_f(\mathbf{u}, p, \boldsymbol{\omega}, \mathbf{v}) = \int_{\Omega_f} \left(\boldsymbol{\sigma}_f(\mathbf{u}, p) : \nabla \mathbf{v} + \rho_f(\mathbf{u} - \boldsymbol{\omega}) \cdot \nabla \mathbf{u} \cdot \mathbf{v} - \rho_f(\nabla \cdot \boldsymbol{\omega}) \mathbf{u} \cdot \mathbf{v} + \frac{\rho_f}{2}(\nabla \cdot \mathbf{u}) \mathbf{u} \cdot \mathbf{v} \right) dx - \int_{\Gamma_f^{\text{neu}}} \mathbf{g}_f^{\text{neu}} \cdot \mathbf{v} \, dx; \\ b_f(\mathbf{u}, q) = - \int_{\Omega_f} (\nabla \cdot \mathbf{u}) q \, dx; \\ R'_s(\tilde{\mathbf{d}}, \tilde{\mathbf{w}}) = \int_{\tilde{\Omega}_s} \left(\tilde{\boldsymbol{\Pi}}_s(\tilde{\mathbf{d}}) : \tilde{\nabla} \tilde{\mathbf{w}} \right) dx - \int_{\tilde{\Gamma}_s^{\text{neu}}} \tilde{\mathbf{g}}_s^{\text{neu}} \cdot \tilde{\mathbf{w}} \, dx. \end{cases} \quad (6b)$$

We use a prime to indicate that the residuals R'_f and R'_s contain only spatial contributions, that is, no time derivatives. We shall use R_f and R_s to refer to the corresponding full residuals that include both temporal and spatial terms. We add the strongly consistent term $\frac{\rho_f}{2}(\nabla \cdot \mathbf{u}) \mathbf{u} \cdot \mathbf{v}$ to the fluid residual in $(6b)_1$ to ensure the energy balance at the semi-discrete level [62, 49].

2.3 Semi-discrete formulation

We now introduce a finite element semi-discretization of the weak FSI problem. We adopt a nodal $\mathbb{P}_\kappa - \mathbb{P}_{\kappa-1}$ Taylor-Hood finite element (FE) discretization for the fluid and a \mathbb{P}_κ FE discretization for the solid. Let $\{\phi_i^f\}_{i=1}^{N_u}$, $\{\theta_i^f\}_{i=1}^{N_p}$ and $\{\varphi_i^s\}_{i=1}^{N_s}$ denote the nodal basis functions for the fluid velocity, fluid pressure and solid displacement,

respectively. We introduce the vectors of finite element coefficients $\mathbf{u}_f : (0, T] \rightarrow \mathbb{R}^{N_u}$, $\mathbf{p}_f : (0, T] \rightarrow \mathbb{R}^{N_p}$, $\mathbf{d}_s : (0, T] \rightarrow \mathbb{R}^{N_s}$, and define the associated finite element approximations by

$$\begin{aligned} \mathbf{u}_{f,h}(\mathbf{x}, t) &= \sum_{j=1}^{N_u} (\mathbf{u}_f(t))_j \phi_j^f(\mathbf{x}, t), & p_{f,h}(\mathbf{x}, t) &= \sum_{j=1}^{N_p} (\mathbf{p}_f(t))_j \theta_j^f(\mathbf{x}, t), & \mathbf{x} &\in \Omega_f(t); \\ \tilde{\mathbf{d}}_{s,h}(\tilde{\mathbf{x}}, t) &= \sum_{j=1}^{N_s} (\mathbf{d}_s(t))_j \varphi_j^s(\tilde{\mathbf{x}}), & & & \tilde{\mathbf{x}} &\in \tilde{\Omega}_s. \end{aligned} \quad (7)$$

Next, we define the fluid and solid mass matrices $\mathbf{M}_f \in \mathbb{R}^{N_u \times N_u}$ and $\mathbf{M}_s \in \mathbb{R}^{N_s \times N_s}$ as

$$\begin{aligned} (\mathbf{M}_f)_{ij}(t) &= \int_{\Omega_f(t)} \rho_f \phi_j^f(\mathbf{x}, t) \cdot \phi_i^f(\mathbf{x}, t) dx, & i, j &= 1, \dots, N_u, \\ (\mathbf{M}_s)_{ij} &= \int_{\tilde{\Omega}_s} \tilde{\rho}_s \varphi_j^s(\tilde{\mathbf{x}}) \cdot \varphi_i^s(\tilde{\mathbf{x}}) dx, & i, j &= 1, \dots, N_s, \end{aligned}$$

and the discrete incompressibility constraint matrix $\mathbf{B}_f \in \mathbb{R}^{N_p \times N_u}$

$$(\mathbf{B}_f)_{ij} = - \int_{\Omega_f(t)} (\nabla \cdot \phi_j^f(\mathbf{x}, t)) \theta_i^f(\mathbf{x}, t) dx, \quad i = 1, \dots, N_p, j = 1, \dots, N_u.$$

We notice that the matrices \mathbf{B}_f and \mathbf{M}_f depend on the interface displacement field $\tilde{\mathbf{d}}_{s,h}|_{\tilde{\Gamma}}$ through the morphing. We also define Boolean mask matrices $\mathbf{P}_{\bullet,\Gamma}, \mathbf{P}_{\bullet,\text{in}}, \mathbf{P}_{\bullet,\text{dir}}$ associated with the interface, the internal and the Dirichlet degrees of freedom, respectively, for the fluid ($\bullet = f$) and the solid ($\bullet = s$) subdomains. For example, $\mathbf{P}_{f,\Gamma} \mathbf{u}_f \in \mathbb{R}^{N_c}$ collects the fluid velocity DOFs at the fluid-structure interface $\Gamma(t)$, where N_c is the number of DOFs at the interface. Moreover, we introduce the fluid residual vector $\mathbf{R}'_f(\mathbf{u}_f, \mathbf{p}_f, \mathbf{P}_{s,\Gamma} \mathbf{d}_s) \in \mathbb{R}^{N_u}$, which collects all spatial contributions of the semi-discrete fluid momentum equation (diffusion, pressure, convection, etc.)

$$\begin{aligned} (\mathbf{R}'_f(\mathbf{u}_f, \mathbf{p}_f, \mathbf{P}_{s,\Gamma} \mathbf{d}_s))_i &= \int_{\Omega_f(t)} \left(2\mu_f \varepsilon_f(\mathbf{u}_{f,h}) : \varepsilon_f(\phi_i^f) - p_{f,h} \nabla \cdot \phi_i^f + \rho_f [(\mathbf{u}_{f,h} - \boldsymbol{\omega}_{f,h}) \cdot \nabla] \mathbf{u}_{f,h} \cdot \phi_i^f \right. \\ &\quad \left. - \rho_f (\nabla \cdot \boldsymbol{\omega}_{f,h}) \mathbf{u}_{f,h} \cdot \phi_i^f + \frac{\rho_f}{2} (\nabla \cdot \mathbf{u}_{f,h}) \mathbf{u}_{f,h} \cdot \phi_i^f \right) dx - \int_{\Gamma_f^{\text{neu}}(t)} \mathbf{g}_f^{\text{neu}} \cdot \phi_i^f dx, \end{aligned} \quad (8)$$

$i = 1, \dots, N_u.$

Similarly, the solid residual vector $\mathbf{R}'_s(\mathbf{d}_s) \in \mathbb{R}^{N_s}$ is defined as

$$(\mathbf{R}'_s(\mathbf{d}_s))_i = \int_{\tilde{\Omega}_s} \tilde{\Pi}_s(\tilde{\mathbf{d}}_{s,h}) : \tilde{\nabla} \varphi_i^s dx - \int_{\tilde{\Gamma}_s^{\text{neu}}} \tilde{\mathbf{g}}_s^{\text{neu}} \cdot \varphi_i^s dx, \quad i = 1, \dots, N_s. \quad (9)$$

The semi-discrete FSI equations in algebraic form can now be expressed as

$$\left\{ \begin{array}{l} \mathbf{P}_{f,\Gamma} \left[\frac{d(\mathbf{M}_f \mathbf{u}_f)}{dt} + \mathbf{R}'_f(\mathbf{u}_f, \mathbf{p}_f, \mathbf{P}_{s,\Gamma} \mathbf{d}_s) \right] + \mathbf{P}_{s,\Gamma} \left[\mathbf{M}_s \ddot{\mathbf{d}}_s + \mathbf{R}'_s(\mathbf{d}_s) \right] = 0; \\ \mathbf{P}_{f,\Gamma} \mathbf{u}_f = \mathbf{P}_{s,\Gamma} \dot{\mathbf{d}}_s; \\ \mathbf{P}_{f,\text{in}} \left[\frac{d(\mathbf{M}_f \mathbf{u}_f)}{dt} + \mathbf{R}'_f(\mathbf{u}_f, \mathbf{p}_f, \mathbf{P}_{s,\Gamma} \mathbf{d}_s) \right] = 0; \\ \mathbf{B}_f \mathbf{u}_f = 0; \\ \mathbf{P}_{s,\text{in}} \left[\mathbf{M}_s \ddot{\mathbf{d}}_s + \mathbf{R}'_s(\mathbf{d}_s) \right] = 0; \\ \mathbf{P}_{f,\text{dir}} \mathbf{u}_f = \mathbf{u}_{f,\text{dir}}, \quad \mathbf{P}_{s,\text{dir}} \mathbf{d}_s = \mathbf{d}_{s,\text{dir}}. \end{array} \right. \quad (10)$$

Equations (10)₁-(10)₂ correspond to the weak form of the dynamic equilibrium and the strong form of the kinematic continuity of velocities at the interface. Equations (10)₃-(10)₅ represent the semi-discrete fluid and solid balance equations within their respective interior domains, and (10)₆ enforces the Dirichlet boundary conditions.

We now rewrite the coupled semi-discrete FSI system (10) into an abstract differential-algebraic form, which will allow us to directly apply the implicit Runge-Kutta scheme introduced later in Section 3.1. To this end, we first introduce the structural velocity

$$\mathbf{u}_s(t) := \dot{\mathbf{d}}_s(t),$$

so that the second-order structural equation is transformed into an equivalent first-order form. We define the masked momentum variables by

$$\mathbf{y}_\Gamma := \mathbf{P}_{f,\Gamma} \mathbf{M}_f \mathbf{u}_f + \mathbf{P}_{s,\Gamma} \mathbf{M}_s \mathbf{u}_s, \quad \mathbf{y}_{f,\text{in}} := \mathbf{P}_{f,\text{in}} \mathbf{M}_f \mathbf{u}_f, \quad \mathbf{y}_{s,\text{in}} := \mathbf{P}_{s,\text{in}} \mathbf{M}_s \mathbf{u}_s,$$

and collect them, along with the structural displacement, into the differential state vector

$$\mathbf{y}(t) := \text{col}(\mathbf{y}_\Gamma(t), \mathbf{y}_{f,\text{in}}(t), \mathbf{y}_{s,\text{in}}(t), \mathbf{d}_s(t)).$$

The fluid pressure degrees of freedom are treated as algebraic variables and collected into

$$\mathbf{z}(t) := \mathbf{p}_f(t).$$

With these definitions, the coupled semi-discrete FSI system (10) can be compactly expressed as the differential-algebraic equations

$$\begin{cases} \dot{\mathbf{y}}(t) = \mathbf{f}(t, \mathbf{y}(t), \mathbf{z}(t)), \\ \mathbf{0} = \mathbf{g}(t, \mathbf{y}(t)), \end{cases} \quad (11)$$

where the right-hand side of the differential equation is given by

$$\begin{aligned} \mathbf{f}_1 &= -\mathbf{P}_{f,\Gamma} \mathbf{R}'_f(\mathbf{u}_f(t, \mathbf{y}), \mathbf{z}, \mathbf{P}_{s,\Gamma} \mathbf{d}_s) - \mathbf{P}_{s,\Gamma} \mathbf{R}'_s(\mathbf{d}_s), \\ \mathbf{f}_2 &= -\mathbf{P}_{f,\text{in}} \mathbf{R}'_f(\mathbf{u}_f(t, \mathbf{y}), \mathbf{z}, \mathbf{P}_{s,\Gamma} \mathbf{d}_s), \\ \mathbf{f}_3 &= -\mathbf{P}_{s,\text{in}} \mathbf{R}'_s(\mathbf{d}_s), \\ \mathbf{f}_4 &= \mathbf{u}_s(t, \mathbf{y}), \end{aligned}$$

and the algebraic constraints $\mathbf{g}(t, \mathbf{y}) = \mathbf{0}$ contains the remaining equations (10)₂, (10)₄, and (10)₆, which do not involve time derivatives.

Remark 2.1. *The Boolean mask matrices $(\mathbf{P}_{f,\Gamma}, \mathbf{P}_{f,\text{in}}, \mathbf{P}_{f,\text{dir}})$ and $(\mathbf{P}_{s,\Gamma}, \mathbf{P}_{s,\text{in}}, \mathbf{P}_{s,\text{dir}})$ define a partition of the fluid and solid degrees of freedom. For fixed Dirichlet boundary data $\mathbf{u}_{f,\text{dir}}(t)$ and $\mathbf{d}_{s,\text{dir}}(t)$, the masked momentum variables $(\mathbf{y}_\Gamma, \mathbf{y}_{f,\text{in}}, \mathbf{y}_{s,\text{in}})$ uniquely determine the free fluid and structural velocities. Therefore, we regard \mathbf{u}_f and \mathbf{u}_s as functions of the differential state $\mathbf{y}(t)$ and of time, and we write*

$$\mathbf{u}_f = \mathbf{u}_f(t, \mathbf{y}), \quad \mathbf{u}_s = \mathbf{u}_s(t, \mathbf{y})$$

for brevity.

3 Implicit Runge-Kutta time integration

3.1 Fully-discrete formulation

This section introduces the fully discrete formulation of the FSI problem based on an implicit Runge-Kutta (IRK) temporal discretization. We first recall the general IRK framework and introduce the relevant notation. We then apply the IRK scheme to the coupled differential-algebraic system introduced in Section 2.3. Finally, we assemble the fully discrete coupled system into a compact monolithic form suitable for numerical solution.

Consider a general ordinary differential equation (ODE) of the form $\frac{d\mathbf{y}}{dt} = \mathbf{f}(t, \mathbf{y})$. An s -stage IRK discretization is characterized by the Butcher tableau $(\mathbf{A}, \mathbf{b}, \mathbf{c})$

$$\begin{array}{c|cccc} c_1 & a_{11} & a_{12} & \cdots & a_{1s} \\ c_2 & a_{21} & a_{22} & \cdots & a_{2s} \\ \vdots & \vdots & & \ddots & \vdots \\ c_s & a_{s1} & a_{s2} & \cdots & a_{ss} \\ \hline & b_1 & b_2 & \cdots & b_s \end{array} \quad (12)$$

Given the state $\mathbf{y}^{(n)}$, we define $\mathbf{y}^{(n+1)}$ at time $t_{n+1} = t_n + \Delta t$ as follows

$$\mathbf{y}^{(n+1)} = \mathbf{y}^{(n)} + \Delta t \sum_{i=1}^s b_i \mathbf{k}_i, \quad \mathbf{k}_i = \mathbf{f} \left(t_n + c_i \Delta t, \mathbf{y}^{(n)} + \Delta t \sum_{j=1}^s a_{ij} \mathbf{k}_j \right), \quad i = 1, \dots, s. \quad (13)$$

In principle, (13) can be directly solved as a nonlinear system involving the stage increments $\{\mathbf{k}_i\}_{i=1}^s$. However, it is beneficial for computational implementation to reformulate the method in terms of intermediate stage

states explicitly. This equivalent formulation facilitates the definition of consistent residuals at the discrete level in the FSI problem. Towards this end, we introduce the stage times $t^{(n+c_i)} := t_n + c_i \Delta t$ and the stage states $\mathbf{y}^{(n+c_i)} := \mathbf{y}^{(n)} + \Delta t \sum_{j=1}^s a_{ij} \mathbf{k}_j$. The elimination of the stage increments \mathbf{k}_j in (13) yields the equivalent stage form

$$\mathbf{y}^{(n+c_i)} = \mathbf{y}^{(n)} + \Delta t \sum_{j=1}^s a_{ij} \mathbf{f} \left(t^{(n+c_j)}, \mathbf{y}^{(n+c_j)} \right) \quad \text{for } i = 1, \dots, s, \quad (14)$$

for the intermediate states $\{\mathbf{y}^{(n+c_i)}\}_i$, which is followed by the projection step to define the next state $\mathbf{y}^{(n+1)}$,

$$\mathbf{y}^{(n+1)} = \mathbf{y}^{(n)} + \Delta t \sum_{i=1}^s b_i \mathbf{f} \left(t^{(n+c_i)}, \mathbf{y}^{(n+c_i)} \right). \quad (15)$$

In this work, we adopt Radau-IIA IRK methods [38, 31, 29], which are stiffly accurate: $a_{si} = b_i$ ($i = 1, \dots, s$) and $c_s = 1$. Consequently, the final stage coincides with the step solution, $\mathbf{y}^{(n+1)} = \mathbf{y}^{(n+c_s)}$, and the separate projection step (15) can be omitted.

We now apply the IRK time integration to the semi-discrete FSI system (11), and obtain the component-wise stage equations

$$\left\{ \begin{array}{l} \mathbf{y}_\Gamma^{(n+c_i)} = \mathbf{y}_\Gamma^{(n)} - \Delta t \sum_{j=1}^s a_{ij} \left[\mathbf{P}_{f,\Gamma} \mathbf{R}'_f(\mathbf{u}_f^{(n+c_j)}, \mathbf{p}_f^{(n+c_j)}, \mathbf{P}_{s,\Gamma} \mathbf{d}_s^{(n+c_j)}) + \mathbf{P}_{s,\Gamma} \mathbf{R}'_s(\mathbf{d}_s^{(n+c_j)}) \right], \\ \mathbf{y}_{f,\text{in}}^{(n+c_i)} = \mathbf{y}_{f,\text{in}}^{(n)} - \Delta t \sum_{j=1}^s a_{ij} \mathbf{P}_{f,\text{in}} \mathbf{R}'_f(\mathbf{u}_f^{(n+c_j)}, \mathbf{p}_f^{(n+c_j)}, \mathbf{P}_{s,\Gamma} \mathbf{d}_s^{(n+c_j)}), \\ \mathbf{y}_{s,\text{in}}^{(n+c_i)} = \mathbf{y}_{s,\text{in}}^{(n)} - \Delta t \sum_{j=1}^s a_{ij} \mathbf{P}_{s,\text{in}} \mathbf{R}'_s(\mathbf{d}_s^{(n+c_j)}), \\ \mathbf{d}_s^{(n+c_i)} = \mathbf{d}_s^{(n)} + \Delta t \sum_{j=1}^s a_{ij} \mathbf{u}_s^{(n+c_j)}, \\ \mathbf{P}_{f,\Gamma} \mathbf{u}_f^{(n+c_i)} = \mathbf{P}_{s,\Gamma} \mathbf{u}_s^{(n+c_i)}, \\ \mathbf{B}_f \mathbf{u}_f^{(n+c_i)} = \mathbf{0}, \\ \mathbf{P}_{f,\text{dir}} \mathbf{u}_f^{(n+c_i)} = \mathbf{u}_{f,\text{dir}}^{(n+c_i)}, \quad \mathbf{P}_{f,\text{dir}} \mathbf{d}_s^{(n+c_i)} = \mathbf{d}_{f,\text{dir}}^{(n+c_i)}, \end{array} \right. \quad (16)$$

If we substitute the definitions of the masked momentum variables (cf. section 2.3),

$$\mathbf{y}_\Gamma^{(\cdot)} = \mathbf{P}_{f,\Gamma} \mathbf{M}_f^{(\cdot)} \mathbf{u}_f^{(\cdot)} + \mathbf{P}_{s,\Gamma} \mathbf{M}_s \mathbf{u}_s^{(\cdot)}, \quad \mathbf{y}_{f,\text{in}}^{(\cdot)} = \mathbf{P}_{f,\text{in}} \mathbf{M}_f^{(\cdot)} \mathbf{u}_f^{(\cdot)}, \quad \mathbf{y}_{s,\text{in}}^{(\cdot)} = \mathbf{P}_{s,\text{in}} \mathbf{M}_s \mathbf{u}_s^{(\cdot)},$$

into the first three relations of (16), and we rearrange the terms, we obtain the discrete fully discrete formulation: at each stage $i = 1, \dots, s$

$$\left\{ \begin{array}{l} \mathbf{P}_{f,\Gamma} \mathbf{R}_f^{(n+c_i)} + \mathbf{P}_{s,\Gamma} \mathbf{R}_s^{(n+c_i)} = 0, \\ \mathbf{P}_{f,\Gamma} \mathbf{u}_f^{(n+c_i)} = \mathbf{P}_{s,\Gamma} \mathbf{u}_s^{(n+c_i)}, \\ \mathbf{P}_{f,\text{in}} \mathbf{R}_f^{(n+c_i)} = 0, \\ \mathbf{B}_f^{(n+c_i)} \mathbf{u}_f^{(n+c_i)} = 0, \\ \mathbf{P}_{s,\text{in}} \mathbf{R}_s^{(n+c_i)} = 0, \\ \mathbf{P}_{f,\text{dir}} \mathbf{u}_f^{(n+c_i)} = \mathbf{u}_{f,\text{dir}}^{(n+c_i)}, \quad \mathbf{P}_{s,\text{dir}} \mathbf{d}_s^{(n+c_i)} = \mathbf{d}_{s,\text{dir}}^{(n+c_i)}, \end{array} \right. \quad (17)$$

where $\mathbf{R}_f^{(n+c_i)}$ and $\mathbf{R}_s^{(n+c_i)}$ denote the fully discrete fluid and solid momentum residuals at the stage time $t^{(n+c_i)}$. Their explicit expressions are provided in A. For completeness, in A we prove that (17) can be obtained by first discretizing the fluid and solid equations separately with the IRK scheme and subsequently enforcing the interface coupling conditions. Both approaches are algebraically equivalent and yield the same fully discrete coupled system.

We further note that the fully discrete formulation (16) involves four differential components in the state vector \mathbf{y} . After applying the IRK scheme, the kinematic stage equations for the displacement $\mathbf{d}_s^{(n+c_i)}$ are used to eliminate the solid stage velocities $\mathbf{u}_s^{(n+c_i)}$ from the solid momentum residual $\mathbf{R}_s^{(n+c_i)}$, for $i = 1, \dots, s$. As a consequence, (16)₄ is implicitly encoded in the definition of $\mathbf{R}_s^{(n+c_i)}$, and the resulting fully discrete stage system (17) is expressed in terms of three momentum blocks plus the algebraic constraints, in direct analogy with the semi-discrete HF formulation (10).

Note that the equations at each IRK stage are not independent; rather, they are inherently coupled across stages through the off-diagonal Butcher tableau coefficients. This inter-stage coupling implies that we need to solve a large implicit nonlinear system that encompass all stages. To explicitly illustrate and address this coupling structure, we introduce stage-stacked vectors. Specifically, we define stage-stacked unknowns as:

$$\mathbf{U}_f := \text{col}(\mathbf{u}_f^{(n+c_1)}, \dots, \mathbf{u}_f^{(n+c_s)}) \in \mathbb{R}^{sN_u}, \quad \mathbf{P}_f := \text{col}(\mathbf{p}_f^{(n+c_1)}, \dots, \mathbf{p}_f^{(n+c_s)}) \in \mathbb{R}^{sN_p},$$

$$\mathbf{D}_s := \text{col}(\mathbf{d}_s^{(n+c_1)}, \dots, \mathbf{d}_s^{(n+c_s)}) \in \mathbb{R}^{sN_s}, \quad \mathbf{U}_s := \text{col}(\mathbf{u}_s^{(n+c_1)}, \dots, \mathbf{u}_s^{(n+c_s)}) \in \mathbb{R}^{sN_s},$$

where the operator $\text{col}(\cdot)$ denotes vertical concatenation. Correspondingly, we also define stage-stacked residual vectors

$$\mathcal{R}_f(\mathbf{U}_f, \mathbf{p}_f, \mathbf{D}_s) := \text{col}(\mathbf{R}_f^{(n+c_1)}, \dots, \mathbf{R}_f^{(n+c_s)}), \quad \mathcal{R}_s(\mathbf{D}_s) := \text{col}(\mathbf{R}_s^{(n+c_1)}, \dots, \mathbf{R}_s^{(n+c_s)}).$$

We further define stage-stacked Boolean mask matrices and the discrete divergence operator:

$$\mathcal{P}_\bullet := I_s \otimes \mathbf{P}_\bullet, \quad \mathcal{B}_f := \text{blkdiag}(\mathbf{B}_f^{(n+c_1)}, \dots, \mathbf{B}_f^{(n+c_s)}),$$

where $I_s \otimes \mathbf{P}_\bullet \in \mathbb{R}^{sN_s^{\text{row}} \times sN_s^{\text{col}}}$ is the Kronecker product of the identity matrix I_s and $\mathbf{P}_\bullet \in \mathbb{R}^{N_s^{\text{row}} \times N_s^{\text{col}}}$,

$$(I_s \otimes \mathbf{P}_\bullet)_{i,j} = (I_s)_{r,q} (\mathbf{P}_\bullet)_{v,w}, \quad i = (r-1)N_s^{\text{row}} + v, \quad j = (q-1)N_s^{\text{col}} + w,$$

with

$$1 \leq r, q \leq s, \quad 1 \leq v \leq N_s^{\text{row}}, \quad 1 \leq w \leq N_s^{\text{col}}.$$

As mentioned previously, the solid velocity variables can be eliminated by substituting the kinematic relation (16)₄ into the solid momentum equations (16)₃ and the interface condition (16)₁: this substitution leads to a formulation that involves only solid displacements as unknowns. In more detail, we find

$$\mathbf{U}_s = \frac{1}{\Delta t} (\mathbf{A}^{-1} \otimes I_{N_s}) \mathbf{D}_s - \frac{1}{\Delta t} ((\mathbf{A}^{-1} \mathbf{1}_s) \otimes I_{N_s}) \mathbf{d}_s^{(n)},$$

where $\mathbf{A} \in \mathbb{R}^{s \times s}$ is the Butcher matrix associated with the RK scheme and $\mathbf{1}_s \in \mathbb{R}^s$ is the vector of ones. For simplicity, we rewrite this relation compactly as

$$\mathbf{U}_s = \mathcal{D}_{s,\Delta t} \mathbf{D}_s. \quad (18)$$

Note that the discrete time differentiation operator $\mathcal{D}_{s,\Delta t}$ changes at each time step; in the remainder, we omit this explicit dependence to shorten notation.

With the definitions and notation established above, we can now formulate the global fully discrete monolithic system, which couples all IRK stages simultaneously. At each time step, the fully discrete FSI problem consists of solving for the stacked unknowns $(\mathbf{U}_f, \mathbf{p}_f, \mathbf{D}_s)$:

$$\begin{cases} \mathcal{P}_{f,\Gamma} \mathcal{R}_f(\mathbf{U}_f, \mathbf{p}_f, \mathcal{P}_{s,\Gamma} \mathbf{D}_s) + \mathcal{P}_{s,\Gamma} \mathcal{R}_s(\mathbf{D}_s) = 0, \\ \mathcal{P}_{f,\Gamma} \mathbf{U}_f = \mathcal{P}_{s,\Gamma} \mathbf{U}_s, \\ \mathcal{P}_{f,\text{in}} \mathcal{R}_f(\mathbf{U}_f, \mathbf{p}_f, \mathcal{P}_{s,\Gamma} \mathbf{D}_s) = 0, \\ \mathcal{B}_f \mathbf{U}_f = 0, \\ \mathcal{P}_{s,\text{in}} \mathcal{R}_s(\mathbf{D}_s) = 0, \\ \mathcal{P}_{f,\text{dir}} \mathbf{U}_f = \mathbf{U}_{f,\text{dir}}, \quad \mathcal{P}_{s,\text{dir}} \mathbf{D}_s = \mathbf{D}_{s,\text{dir}}. \end{cases} \quad (19)$$

Note that (19) shares the same structure with the standard BDF-Newmark implicit time discretization of FSI problems, but it has s -times more equations and unknowns. Eq. (19)₁ enforces dynamic equilibrium of normal stresses at the fluid-structure interface, Eq. (19)₂ enforces kinematic continuity (matching of normal velocities) at the interface, and the remaining equations impose the fluid and solid governing equations in the interior together with Dirichlet boundary conditions.

3.2 Solution to the fully discrete FSI system (19)

In order to describe the application of static condensation to (19), we introduce notation:

$$\mathbf{g} := \mathcal{P}_{s,\Gamma} \mathbf{D}_s, \quad \mathbf{W}_f := \text{col}(\mathcal{P}_{f,\text{in}} \mathbf{U}_f, \mathbf{p}_f), \quad \mathbf{D}_s^{\text{in}} := \mathcal{P}_{s,\text{in}} \mathbf{D}_s. \quad (20)$$

Recalling (18) and the kinematic condition (19)₂, we find that \mathbf{U}_f is uniquely determined by \mathbf{W}_f , \mathbf{g} and the solution at the previous time step; similarly, \mathbf{D}_s is uniquely determined by \mathbf{D}_s^{in} and \mathbf{g} . We can hence introduce the residuals:

$$\begin{cases} \mathcal{R}_\Gamma(\mathbf{W}_f, \mathbf{g}, \mathbf{D}_s^{\text{in}}) := \mathcal{P}_{f,\Gamma} \mathcal{R}_f(\mathbf{U}_f, \mathbf{p}_f, \mathcal{P}_{s,\Gamma} \mathbf{D}_s) + \mathcal{P}_{s,\Gamma} \mathcal{R}_s(\mathbf{D}_s), \\ \mathcal{R}_{s,\text{in}}(\mathbf{D}_s^{\text{in}}, \mathbf{g}) := \begin{bmatrix} \mathcal{P}_{s,\text{in}} \mathcal{R}_s(\mathbf{D}_s) \\ \mathcal{P}_{s,\text{dir}} \mathbf{D}_s - \mathbf{D}_{s,\text{dir}} \end{bmatrix}, \quad \mathcal{R}_{f,\text{in}}(\mathbf{W}_f, \mathbf{g}) := \begin{bmatrix} \mathcal{P}_{f,\text{in}} \mathcal{R}_f(\mathbf{U}_f, \mathbf{p}_f, \mathcal{P}_{s,\Gamma} \mathbf{D}_s) \\ \mathcal{B}_{f,\Gamma} \mathbf{U}_f \\ \mathcal{P}_{f,\text{dir}} \mathbf{U}_f - \mathbf{U}_{f,\text{dir}} \end{bmatrix}. \end{cases} \quad (21)$$

In conclusion, we rewrite (19) as

$$\begin{cases} \mathcal{R}_\Gamma(\mathbf{W}_f, \mathbf{g}, \mathbf{D}_s^{\text{in}}) = 0, \\ \mathcal{R}_{s,\text{in}}(\mathbf{D}_s^{\text{in}}, \mathbf{g}) = 0, \\ \mathcal{R}_{f,\text{in}}(\mathbf{W}_f, \mathbf{g}) = 0. \end{cases} \quad (22)$$

If we apply the Newton's method to (22), we obtain

$$\begin{cases} \mathcal{R}_\Gamma^{(j)} + \mathcal{J}_{\Gamma,f} \delta \mathbf{W}_f + \mathcal{J}_{\Gamma,s} \delta \mathbf{D}_s^{\text{in}} + \mathcal{J}_{\Gamma,g} \delta \mathbf{g} = 0, & \text{where } \mathcal{J}_{\Gamma,f} = \frac{\partial \mathcal{R}_\Gamma^{(j)}}{\partial \mathbf{W}_f}, \quad \mathcal{J}_{\Gamma,s} = \frac{\partial \mathcal{R}_\Gamma^{(j)}}{\partial \mathbf{D}_s^{\text{in}}}, \quad \mathcal{J}_{\Gamma,g} = \frac{\partial \mathcal{R}_\Gamma^{(j)}}{\partial \mathbf{g}}; \\ \mathcal{R}_{s,\text{in}}^{(j)} + \mathcal{J}_{s,s} \delta \mathbf{D}_s^{\text{in}} + \mathcal{J}_{s,g} \delta \mathbf{g} = 0, & \text{where } \mathcal{J}_{s,s} = \frac{\partial \mathcal{R}_{s,\text{in}}^{(j)}}{\partial \mathbf{D}_s^{\text{in}}}, \quad \mathcal{J}_{s,g} = \frac{\partial \mathcal{R}_{s,\text{in}}^{(j)}}{\partial \mathbf{g}}; \\ \mathcal{R}_{f,\text{in}}^{(j)} + \mathcal{J}_{f,f} \delta \mathbf{W}_f + \mathcal{J}_{f,g} \delta \mathbf{g} = 0, & \text{where } \mathcal{J}_{f,f} = \frac{\partial \mathcal{R}_{f,\text{in}}^{(j)}}{\partial \mathbf{W}_f}, \quad \mathcal{J}_{f,g} = \frac{\partial \mathcal{R}_{f,\text{in}}^{(j)}}{\partial \mathbf{g}}; \end{cases} \quad (23)$$

and j denotes the Newton's iteration. The latter system can be solved using static condensation: first, we exploit the second and the third equations to express the local fluid and the solid states in terms of the interface control $\delta \mathbf{g}$,

$$\begin{cases} \delta \mathbf{D}_s^{\text{in}} = \mathbf{D}_\star^{(j)} + \mathcal{J}_{g \rightarrow s}^{(j)} \delta \mathbf{g} & \text{where } \mathbf{D}_\star^{(j)} = - \left(\mathcal{J}_{s,s}^{(j)} \right)^{-1} \mathcal{R}_{s,\text{in}}^{(j)}, \quad \mathcal{J}_{g \rightarrow s}^{(j)} = - \left(\mathcal{J}_{s,s}^{(j)} \right)^{-1} \mathcal{J}_{s,g}^{(j)}; \\ \delta \mathbf{W}_f = \mathbf{W}_\star^{(j)} + \mathcal{J}_{g \rightarrow f}^{(j)} \delta \mathbf{g} & \text{where } \mathbf{W}_\star^{(j)} = - \left(\mathcal{J}_{f,f}^{(j)} \right)^{-1} \mathcal{R}_{f,\text{in}}^{(j)}, \quad \mathcal{J}_{g \rightarrow f}^{(j)} = - \left(\mathcal{J}_{f,f}^{(j)} \right)^{-1} \mathcal{J}_{f,g}^{(j)}; \end{cases} \quad (24a)$$

next, we substitute the expressions for $\delta \mathbf{D}_s^{\text{in}}$ and $\delta \mathbf{W}_f$ in the first equation to find an independent linear system for the interface control $\delta \mathbf{g}$:

$$\mathcal{S}_{\text{sc}}^{(j)} \delta \mathbf{g} = \mathcal{R}_{\text{sc}}^{(j)}, \quad \text{where} \quad \begin{cases} \mathcal{S}_{\text{sc}}^{(j)} = \mathcal{J}_{\Gamma,g}^{(j)} - \mathcal{J}_{\Gamma,s}^{(j)} \mathcal{J}_{g \rightarrow s}^{(j)} - \mathcal{J}_{\Gamma,f}^{(j)} \mathcal{J}_{g \rightarrow f}^{(j)}, \\ \mathcal{R}_{\text{sc}}^{(j)} = -\mathcal{R}_\Gamma^{(j)} - \mathcal{J}_{\Gamma,s}^{(j)} \mathbf{D}_\star^{(j)} - \mathcal{J}_{\Gamma,f}^{(j)} \mathbf{W}_\star^{(j)}. \end{cases} \quad (24b)$$

In conclusion, at each Newton's iteration, we first compute $\mathbf{D}_\star^{(j)}$, $\mathcal{J}_{g \rightarrow s}^{(j)}$ and $\mathbf{W}_\star^{(j)}$, $\mathcal{J}_{g \rightarrow f}^{(j)}$ using (24a); next, we compute $\delta \mathbf{g}$ using (24b); finally, we compute $\delta \mathbf{D}_s^{\text{in}}$ and $\delta \mathbf{W}_f$ using again (24a).

We can interpret the solution to (22) as the solution to the constrained minimization statement:

$$\min_{\mathbf{W}_f, \mathbf{g}, \mathbf{D}_s^{\text{in}}} \|\mathcal{R}_\Gamma(\mathbf{W}_f, \mathbf{g}, \mathbf{D}_s^{\text{in}})\|_2 \quad \text{subject to} \quad \begin{cases} \mathcal{R}_{s,\text{in}}(\mathbf{D}_s^{\text{in}}, \mathbf{g}) = 0, \\ \mathcal{R}_{f,\text{in}}(\mathbf{W}_f, \mathbf{g}) = 0. \end{cases} \quad (25)$$

Interestingly, if we apply the same sequential quadratic programming (SQP) method as in [48, 49] to (25), at each iteration we find the linear problem (23). Note, however, that while (22) critically relies on the assumption that the fluid and the solid meshes are conforming at the interface, the minimization statement (25) can be readily generalized to non-conforming grids.

4 Model order reduction

In this section, we construct a reduced-order model (ROM) for the FSI problem that preserves the semi-discrete energy balance and the interface coupling structure of the full-order formulation. We first introduce suitable reduced spaces constructed from high-fidelity snapshots using proper orthogonal decomposition (POD). The construction of the reduced spaces follows the bubble-pore decomposition approach as in the static-condensation reduced basis element (scrBE) method [13, 40, 42]. We then derive the semi-discrete ROM and prove an energy balance analogous to the full-order model. Finally, we extend the ROM formulation to the fully discrete IRK setting and discuss the resolution of the ROM.

4.1 Reduced spaces

High-fidelity snapshots are collected at each physical time step $k = 0, \dots, k_{\text{max}}$ and for each IRK stage $i = 1, \dots, s$, i.e., we consider the dataset

$$\left\{ \mathbf{u}_f^{(k+c_i)}, p_f^{(k+c_i)}, \mathbf{d}_s^{(k+c_i)} \right\}_{k=0, \dots, k_{\text{max}}, i=1, \dots, s},$$

where $\mathbf{u}_f^{(k+c_i)} \in \mathbb{R}^{N_u}$ and $p_f^{(k+c_i)} \in \mathbb{R}^{N_p}$ denote the discrete fluid velocity and pressure, and $\mathbf{d}_s^{(k+c_i)} \in \mathbb{R}^{N_s}$ the discrete solid displacement. For long-time integration, we do not store the solution at all time steps to control memory costs.

We rely on POD [63, 64] to construct the reduced-order spaces. We first build the port (interface) space: we collect interface displacement snapshots $\mathbf{d}_{s,\Gamma}^{(k+c_i)} := \mathbf{P}_{s,\Gamma} \mathbf{d}_s^{(k+c_i)} \in \mathbb{R}^{N_c}$, and apply POD based on the $L^2(\tilde{\Gamma})$ -inner product to obtain the interface modes $\{\boldsymbol{\psi}_j\}_{j=1}^m \subset \mathbb{R}^{N_c}$. Each interface mode $\boldsymbol{\psi}_j$ is then harmonically extended into both the fluid and solid domains to construct the *port bases*. Specifically, for each $j = 1, \dots, m$ we solve a Laplace problem with Dirichlet data $\boldsymbol{\psi}_j$ on Γ and homogeneous Dirichlet conditions on the remaining domain boundaries, for both the fluid and solid domains. We denote these resulting discrete fields by $\mathbf{e}_{s,j} \in \mathbb{R}^{N_s}$ and $\mathbf{e}_{f,j} \in \mathbb{R}^{N_u}$, respectively. We collect these fields column-wise to obtain the port basis matrices:

$$\mathbf{E}_s := [\mathbf{e}_{s,1} \cdots \mathbf{e}_{s,m}] \in \mathbb{R}^{N_s \times m}, \quad \mathbf{E}_f := [\mathbf{e}_{f,1} \cdots \mathbf{e}_{f,m}] \in \mathbb{R}^{N_u \times m}.$$

By construction, each column of \mathbf{E}_s shares the same trace on $\Gamma(t)$ with the corresponding column of \mathbf{E}_f .

We next define *bubble spaces* for the fluid velocity and solid displacement. These spaces describe interior fields that satisfy homogeneous conditions at the interface and on the external Dirichlet boundaries. For the fluid velocity, we assume that the time-dependent Dirichlet boundary data on $\partial\Omega_f(t) \setminus \Gamma(t)$ are prescribed in separable form $\mathbf{u}_{f,\text{dir}}(t) = c_{\text{dir}}(t) \bar{\mathbf{u}}_f^{\text{dir}}$, where $\bar{\mathbf{u}}_f^{\text{dir}} \in \mathbb{R}^{N_u}$ is a fixed spatial lifting function obtained as the harmonic extension of a reference boundary profile. More specifically, $\bar{\mathbf{u}}_f^{\text{dir}}$ solves a Laplace problem with Dirichlet data equal to the reference boundary profile on $\partial\Omega_f \setminus \Gamma$ and homogeneous Dirichlet conditions on Γ . In addition, we introduce the fluid harmonic extension operator $\mathcal{H}_{f,\Gamma}$, which maps an interface velocity trace to an interior velocity field with homogeneous Dirichlet data on the remaining boundary. Thus, for each fluid snapshot, we define

$$\mathbf{u}_{f,\Gamma}^{(k+c_i)} := \mathcal{H}_{f,\Gamma}(\mathbf{P}_{f,\Gamma} \mathbf{u}_f^{(k+c_i)}),$$

and subsequently introduce the lifted fluid snapshot

$$\mathbf{u}_{f,\text{lift}}^{(k+c_i)} := \mathbf{u}_f^{(k+c_i)} - c_{\text{dir}}(t^{(k+c_i)}) \bar{\mathbf{u}}_f^{\text{dir}} - \tilde{\mathbf{u}}_{f,\Gamma}^{(k+c_i)}.$$

By construction, this lifted snapshot vanishes on both the external Dirichlet boundaries and the interface $\Gamma(t)$. We rely on the $H^1(\tilde{\Omega}_f)$ POD to devise the fluid velocity bubble basis

$$\mathbf{Z}_f \in \mathbb{R}^{N_u \times n_u}.$$

The number of modes n_u is determined using an energy criterion. Following the same procedure, we construct the lifted solid snapshots and then we obtain the solid bubble basis

$$\mathbf{Z}_s \in \mathbb{R}^{N_s \times n_s},$$

using POD based on the $H^1(\tilde{\Omega}_s)$ inner product. Finally, we define a reduced-order space for the fluid pressure. We store the pressure snapshots $\{p_f^{(k+c_i)}\}$ and apply POD based on the $L^2(\tilde{\Omega}_s)$ inner product to obtain the pressure basis

$$\mathbf{Z}_p \in \mathbb{R}^{N_p \times n_p}.$$

To preserve inf-sup stability at the reduced level for the fluid, we apply a standard supremizer enrichment [65]. For each pressure mode, we compute an associated velocity supremizer by solving a suitable auxiliary problem, and then we augment the velocity bubble basis \mathbf{Z}_f with the resulting n_p supremizer vectors. This enrichment step practically ensures a bounded inf-sup constant at the reduced-order level.

With the above reduced-order spaces defined, we now state the continuous-time reduced approximation ansatz that will be used to construct a semi-discrete ROM. The reduced approximations for the solid displacement, fluid velocity, and fluid pressure read:

$$\hat{\mathbf{d}}_s(t) = \mathbf{Z}_s \alpha_s(t) + \mathbf{E}_s \beta(t), \tag{26a}$$

$$\hat{\mathbf{u}}_f(t) = \bar{\mathbf{u}}_f^{\text{dir}} c_{\text{dir}}(t) + \mathbf{Z}_f \alpha_f(t) + \mathbf{E}_f \dot{\beta}(t), \tag{26b}$$

$$\hat{\mathbf{p}}_f(t) = \mathbf{Z}_p \alpha_p(t), \tag{26c}$$

where the time-dependent generalized coordinates are $\alpha_f(t) \in \mathbb{R}^{n_u}$, $\alpha_s(t) \in \mathbb{R}^{n_s}$, $\alpha_p(t) \in \mathbb{R}^{n_p}$, and $\beta(t) \in \mathbb{R}^m$. The term $\mathbf{E}_s \beta(t)$ explicitly describes the displacement of the fluid-structure interface, whereas $\mathbf{E}_f \dot{\beta}(t)$ represents the fluid velocity field induced by this interface motion. Since \mathbf{E}_s and \mathbf{E}_f share the same trace on $\Gamma(t)$, this choice automatically enforces kinematic compatibility at the interface.

Remark 4.1. *Since the ALE mapping is the solution to a linear parameter- and time-independent pseudo-elasticity problem, Φ_f is an affine function of the port modes. Therefore, its construction and online evaluation is trivial. We notice that if either nonlinear elasticity models for the ALE morphing need to be employed or the problem features geometric parameters, we should treat the mapping as an additional state variable and devise an offline/online strategy accordingly.*

4.2 Semi-discrete ROM

We now insert the reduced approximation (26) into the semi-discrete FSI equations (10) and project onto the port and bubble spaces to derive the semi-discrete ROM. We define the reduced fluid and solid residuals as

$$\widehat{\mathbf{R}}_f(\cdot) := \frac{d}{dt} (\mathbf{M}_f \widehat{\mathbf{u}}_f) + \mathbf{R}'_f(\cdot), \quad \widehat{\mathbf{R}}_s(\cdot) := \mathbf{M}_s \ddot{\widehat{\mathbf{d}}}_s + \mathbf{R}'_s(\cdot).$$

Galerkin projection of the semi-discrete FSI equations onto the port and bubble spaces yields the ROM:

$$\begin{cases} \mathbf{E}_s^\top \widehat{\mathbf{R}}_s + \mathbf{E}_f^\top \widehat{\mathbf{R}}_f = 0, \\ \mathbf{Z}_f^\top \widehat{\mathbf{R}}_f = 0, \quad \mathbf{Z}_p^\top \mathbf{B}_f \widehat{\mathbf{u}}_f = 0, \\ \mathbf{Z}_s^\top \widehat{\mathbf{R}}_s = 0. \end{cases} \quad (27)$$

In this formulation, the first equation corresponds to the dynamic equilibrium condition at the interface, while the second and the third equations enforce the fluid and solid momentum balances, respectively, within their corresponding bubble spaces. The kinematic continuity at the interface is automatically satisfied by construction.

In view of the stability analysis, we provide the variational formulation associated with (27). Towards this end, we introduce the spaces

$$\begin{cases} \widehat{V}_f(t) = \left\{ \tilde{u} \circ \Phi_f^{-1}(t) : \tilde{u} = \bar{u}_f^{\text{dir}} c_{\text{dir}}(t) + \sum_{i=1}^{n_u} \alpha_i \tilde{\zeta}_{f,i} + \sum_{j=1}^m \beta_j \tilde{e}_{f,j}, \beta \in \mathbb{R}^m, \alpha \in \mathbb{R}^{n_u} \right\}, \\ \widehat{V}_{f,0}(t) = \left\{ \tilde{u} \circ \Phi_f^{-1}(t) : \tilde{u} \in \text{span}\{\tilde{\zeta}_{f,i}\}_{i=1}^{n_u} \cup \text{span}\{\tilde{e}_{f,j}\}_{j=1}^m \right\}, \quad \widehat{Q}_f(t) = \left\{ \tilde{q} \circ \Phi_f^{-1}(t) : \tilde{q} \in \text{span}\{\tilde{\zeta}_{p,i}\}_{i=1}^{n_p} \right\}, \\ \widehat{V}_s = \text{span}\{\tilde{\zeta}_{s,i}\}_{i=1}^{n_s} \cup \text{span}\{\tilde{e}_{s,j}\}_{j=1}^m, \end{cases}$$

where $\{\tilde{\zeta}_{f,i}\}_{i=1}^{n_u}$, $\{\tilde{\zeta}_{p,i}\}_{i=1}^{n_p}$, $\{\tilde{\zeta}_{s,i}\}_{i=1}^{n_s}$, $\{\tilde{e}_{f,j}\}_{j=1}^m$, $\{\tilde{e}_{s,j}\}_{j=1}^m$, are the FE fields associated with the POD bases introduced in section 4.1. We denote by $\widehat{\mathbf{u}}_f \in \widehat{V}_f(t)$, $\widehat{\mathbf{p}}_f \in \widehat{Q}_f(t)$, $\widehat{\mathbf{d}}_s \in \widehat{V}_s$ the reduced-order estimates associated with the FE vectors $\widehat{\mathbf{u}}_f \in \mathbb{R}^{N_u}$, $\widehat{\mathbf{p}}_f \in \mathbb{R}^{N_p}$, $\widehat{\mathbf{d}}_s \in \mathbb{R}^{N_s}$ in (26), respectively. For any $t > 0$, the reduced-order estimates satisfy:

$$\begin{cases} \frac{d}{dt} \int_{\Omega_f(t)} \rho_f \widehat{\mathbf{u}}_f \cdot v \, dx + R'_f(\widehat{\mathbf{u}}_f, \widehat{\mathbf{p}}_f, \boldsymbol{\omega}_f, v) + \int_{\Omega_s} \tilde{\rho}_s \frac{\partial^2 \widehat{\mathbf{d}}_s}{\partial t^2} \cdot w \, dx + R'_s(\widehat{\mathbf{d}}_s, w) = 0; \\ b_f(\widehat{\mathbf{u}}_f, q) = 0; \\ \Phi_f|_{\widetilde{\Gamma}} = \mathbf{id} + \widehat{\mathbf{d}}_s|_{\widetilde{\Gamma}}, \quad \widehat{\mathbf{u}}_f \circ \Phi_f|_{\widetilde{\Gamma}} = \frac{\partial \widehat{\mathbf{d}}_s}{\partial t}|_{\widetilde{\Gamma}}, \quad \boldsymbol{\omega}_f = \frac{\partial \Phi_f}{\partial t}, \end{cases} \quad (28)$$

for any $v \in \widehat{V}_{f,0}(t)$, $q \in \widehat{Q}_f(t)$ and $w \in \widehat{V}_s$ such that $v \circ \Phi_f(t)|_{\widetilde{\Gamma}} = w|_{\widetilde{\Gamma}}$. Note that (28) is the Galerkin projection of (6a). Next, we define the kinetic energies in the fluid and the solid domain, and the solid potential:

$$\widehat{T}_f(t) := \frac{1}{2} \int_{\Omega_f(t)} \rho_f |\widehat{\mathbf{u}}_f(t)|^2 \, dx, \quad \widehat{T}_s(t) := \frac{1}{2} \int_{\Omega_s} \rho_s |\partial_t \widehat{\mathbf{d}}_s(t)|^2 \, dx, \quad \widehat{\mathcal{W}}_s(t) := \int_{\Omega_s} W(\widehat{\mathbf{E}}_s) \, dx,$$

where $\widehat{\mathbf{E}}_s$ is the Green-Lagrange tensor associated with the predicted displacement and W is the density of elastic energy associated with the prescribed constitutive model — i.e., $\widetilde{\boldsymbol{\Sigma}}_s = \frac{\partial W}{\partial \mathbf{E}_s}(\widehat{\mathbf{E}}_s)$. Finally, we define the viscous dissipation:

$$\mathcal{D}(\widehat{\mathbf{u}}_f) = 2\mu_f \int_{\Omega_f(t)} \boldsymbol{\varepsilon}_f(\widehat{\mathbf{u}}_f) : \boldsymbol{\varepsilon}_f(\widehat{\mathbf{u}}_f) \, dx.$$

We can now state the following result that states that the semi-discrete ROM solution satisfies the same energy balance as the full-order model.

Lemma 4.2 (ROM semi-discrete energy balance). *Assume that the reduced FSI system (27) is isolated, i.e., $\widehat{\mathbf{u}}_f = 0$ on $\partial\Omega_f(t) \setminus \Gamma(t)$ and $\widetilde{\boldsymbol{\Pi}}_s \widetilde{\mathbf{n}}_s = 0$ on $\partial\widetilde{\Omega}_s \setminus \widetilde{\Gamma}$. Then the reduced-order solution satisfies the energy balance*

$$\frac{d}{dt} (\widehat{T}_f + \widehat{T}_s + \widehat{\mathcal{W}}_s) + \mathcal{D}_f(\widehat{\mathbf{u}}_f) = 0. \quad (29)$$

Proof. The proof is an immediate consequence of Galerkin orthogonality and the ALE transport formula (see, [49, Lemma 1]). We omit the details. \square

4.3 Fully discrete ROM

The reduced bases introduced in Section 4.1 are purely spatial and do not depend on the IRK stage index. For an s -stage integrator we therefore augment them with an identity Kronecker factor:

$$\mathcal{Z}_f := I_s \otimes \mathbf{Z}_f, \quad \mathcal{Z}_s := I_s \otimes \mathbf{Z}_s, \quad \mathcal{Z}_p := I_s \otimes \mathbf{Z}_p, \quad \mathcal{E}_f := I_s \otimes \mathbf{E}_f, \quad \mathcal{E}_s := I_s \otimes \mathbf{E}_s,$$

and denote the stage-stacked reduced coordinates by

$$\boldsymbol{\alpha}_f \in \mathbb{R}^{s n_u}, \quad \boldsymbol{\alpha}_s \in \mathbb{R}^{s n_s}, \quad \boldsymbol{\alpha}_p \in \mathbb{R}^{s n_p}, \quad \boldsymbol{\beta} \in \mathbb{R}^{s m}.$$

Recalling the stacked full-order unknowns $(\mathbf{U}_f, \mathbf{p}_f, \mathbf{D}_s)$ from Section 3.1, we adopt the following fully discrete ROM ansatz

$$\widehat{\mathbf{D}}_s = \mathcal{Z}_s \boldsymbol{\alpha}_s + \mathcal{E}_s \boldsymbol{\beta}, \tag{30a}$$

$$\widehat{\mathbf{U}}_f = (\mathbf{1}_s \otimes \mathbf{u}_f^{\text{dir}}) c_{\text{dir}} + \mathcal{Z}_f \boldsymbol{\alpha}_f + \mathcal{E}_f \mathcal{D}_{s, \Delta t} \boldsymbol{\beta}, \tag{30b}$$

$$\widehat{\mathbf{p}}_f = \mathcal{Z}_p \boldsymbol{\alpha}_p, \tag{30c}$$

where $\mathcal{D}_{s, \Delta t}$ is the discrete time differentiation operator introduced in (18). Note that the port contribution in the fluid velocity and solid displacement automatically enforces the discrete kinematic condition at the interface at each IRK stage.

If we insert the ansatz (30) into the full residual blocks of formulation (19) and we perform Galerkin projection with the stage-extended port and bubble bases, we obtain the s -stage fully-discrete ROM:

$$\begin{cases} \mathcal{E}_s^\top \mathcal{R}_s(\widehat{\mathbf{D}}_s) + \mathcal{E}_f^\top \mathcal{R}_f(\widehat{\mathbf{U}}_f, \widehat{\mathbf{p}}_f, \widehat{\mathbf{D}}_s) = 0, \\ \mathcal{Z}_f^\top \mathcal{R}_f(\widehat{\mathbf{U}}_f, \widehat{\mathbf{p}}_f, \widehat{\mathbf{D}}_s) = 0, \quad \mathcal{Z}_p^\top \mathcal{B}_f \widehat{\mathbf{U}}_f = 0, \\ \mathcal{Z}_s^\top \mathcal{R}_s(\widehat{\mathbf{D}}_s) = 0. \end{cases}$$

The structure is identical to that of the semi-discrete ROM (27), but now all quantities are stage-stacked and evaluated at the IRK stage times.

To solve the fully discrete ROM, we employ the same procedure described in Section 3.2, but now applied within the reduced-order setting. In this context, the control variable is the interface vector of port coordinates, $\boldsymbol{\beta}$. At each Newton iteration, the reduced interface residual and its Jacobian are computed by leveraging the HF residual operators \mathcal{R}_f and \mathcal{R}_s and the associated reduced-order bases \mathcal{Z}_\bullet and \mathcal{E}_\bullet . Each Newton iteration thus involves the solution to the linearized reduced fluid and solid subproblems and the solution to a reduced Schur complement system. This procedure closely follows the methodology described in [13, 40, 42, 43, 44]. We omit the details.

Remark 4.3. *The fully discrete ROM introduced above can equivalently be obtained by first deriving the semi-discrete ROM (27) and then applying the IRK time integration scheme to the reduced system, using the same Butcher tableau as for the full-order model.*

Remark 4.4. *In this work, the velocity basis is enriched through supremizer modes to maintain the inf-sup stability of the ROM. This enrichment procedure is fundamentally different from the reduced-order basis (ROB) enrichment introduced in [48, 49], which aims instead to restore full rank of the reduced Jacobian. As extensively discussed in the scRBE literature, the port-bubble decomposition and Galerkin projection ensure the well-posedness of the ROM for coercive problems, while the flux-based formulation of [48, 49] require a specialized enrichment strategy. We emphasize, however, that this theoretical result strictly applies to strongly coercive cases and does not directly extend to the noncoercive (saddle-point) structure of the incompressible FSI problems. Nevertheless, numerical experiments presented in Section 5 demonstrate that, even for the nonlinear FSI cases considered in this work, the proposed bubble-port construction remains stable and accurate without requiring the ROB enrichment of [48, 49].*

5 Numerical results

5.1 Vertical beam

We consider an incompressible flow that interacts with a slender elastic beam oriented perpendicularly to the free-stream flow direction. The beam is clamped at its bottom end, while its upper part remains free to deform under the fluid loading. The geometric configuration can be found in [49]. No-slip wall boundary conditions

are prescribed on the top and bottom boundaries of the fluid domain. At the inlet, a parabolic velocity profile is imposed with peak velocity $u_\infty = 1$, while homogeneous Neumann boundary conditions are applied at the outlet. The material parameters are chosen as

$$\rho_f = 1, \quad \tilde{\rho}_s = 1.1, \quad E = 10^3, \quad \nu = 0.3, \quad \mu_f = 0.035.$$

The coupled system is integrated until the final time $T = 6$ s.

5.1.1 HF results

Figure 2 shows the horizontal fluid velocity field at three time instants for the Radau-IIA scheme with $s = 2$ stages and time step $\Delta t = 0.05$ s. The beam is progressively bent by the flow, reaches a maximum deflection, and then recovers slightly towards its undeformed configuration.

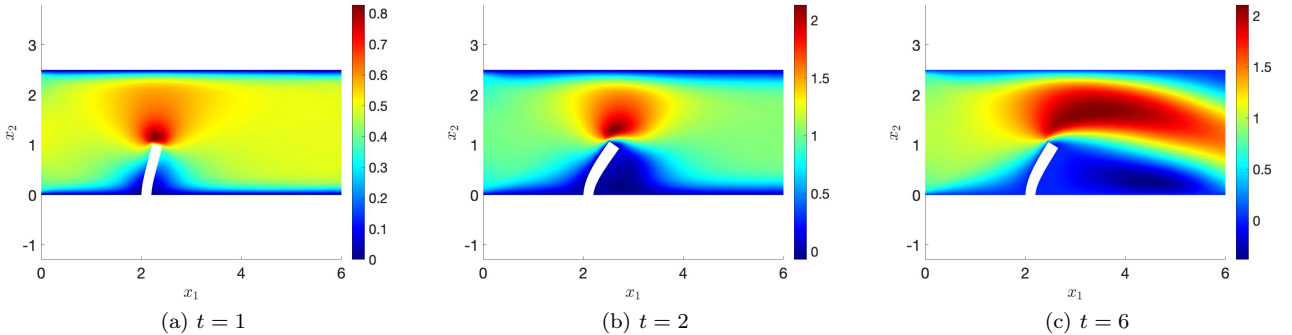


Figure 2: Vertical beam; x -velocity field at 3 time instants ($s = 2$, $\Delta t = 0.05$).

We next investigate the influence of the IRK order and time step on the high-fidelity solution. We perform simulations with $s = 2, 3, 4$ stages and time steps $\Delta t = 0.025, 0.05, 0.1$ s, and monitor the time histories of drag F_x , lift F_y , and the horizontal displacement of a probe point located at the beam tip. Results for $\Delta t = 0.05$ s are reported in Figures 3. Similar results are observed for the other two time steps and all three IRK schemes produce closely matching results. Table 1 reports the H^1 -norm error in the solid displacement for Radau-IIA schemes. Here, the solution obtained with $s = 4$ and time step $\Delta t = 0.001$ is used as the reference solution. For each method, the error increases monotonically with Δt , and an accuracy gain is observed when increasing the number of stages. By performing a least-squares fit to the error data, we estimate effective temporal convergence rates of approximately $p \approx 2.1$, $p \approx 2.4$, and $p \approx 3.5$ for $s = 2, 3, 4$, respectively. The results confirm high-order convergence in time and a systematic accuracy improvement as s increases. The observed convergence rates remain below the formal Radau-IIA orders $2s - 1$: this can be attributed to the differential algebraic structure of the FSI system, where temporal errors interact with spatial discretization of the fluid and solid subproblems, the ALE mesh motion, and the iterative interface-coupling.

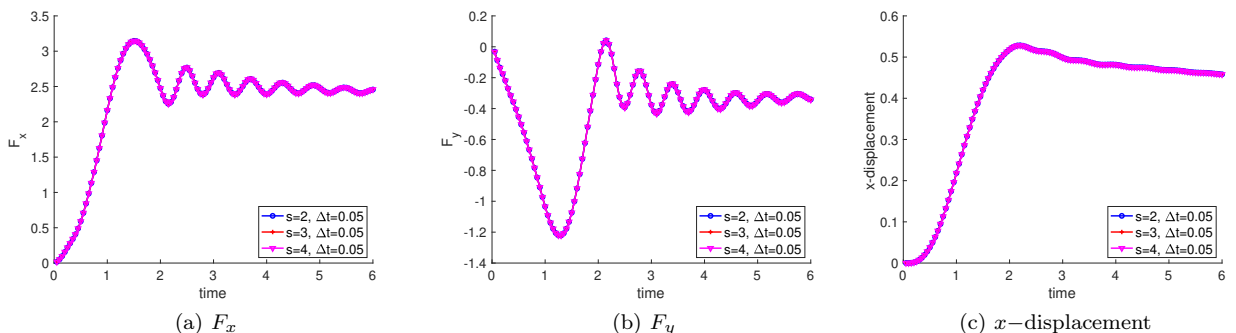


Figure 3: Vertical beam; comparison of fluid forces and tip x -displacement using $s = 2, 3, 4$ and $\Delta t = 0.05$.

$s \backslash \Delta t$	0.025	0.05	0.10
2	7.09×10^{-5}	2.22×10^{-4}	1.32×10^{-3}
3	3.81×10^{-6}	6.55×10^{-5}	1.04×10^{-4}
4	8.52×10^{-7}	6.38×10^{-6}	1.07×10^{-4}

Table 1: Vertical beam; H^1 -norm of the solid displacement error for Radau-IIA schemes with $s = 2, 3, 4$ and time steps $\Delta t = 0.20, 0.10, 0.05$.

5.1.2 ROM results

We first consider ROMs built from $s = 2$ IRK snapshots with time step $\Delta t = 0.05$ s and POD truncation tolerance $\text{tol}_{\text{POD}} = 10^{-5}$. Figure 4 shows the ROM horizontal fluid velocity field and the corresponding pointwise error at $t = 1, 2, 6$ s. The ROM accurately captures the main flow and beam deformation features, and the errors remain small throughout the domain.

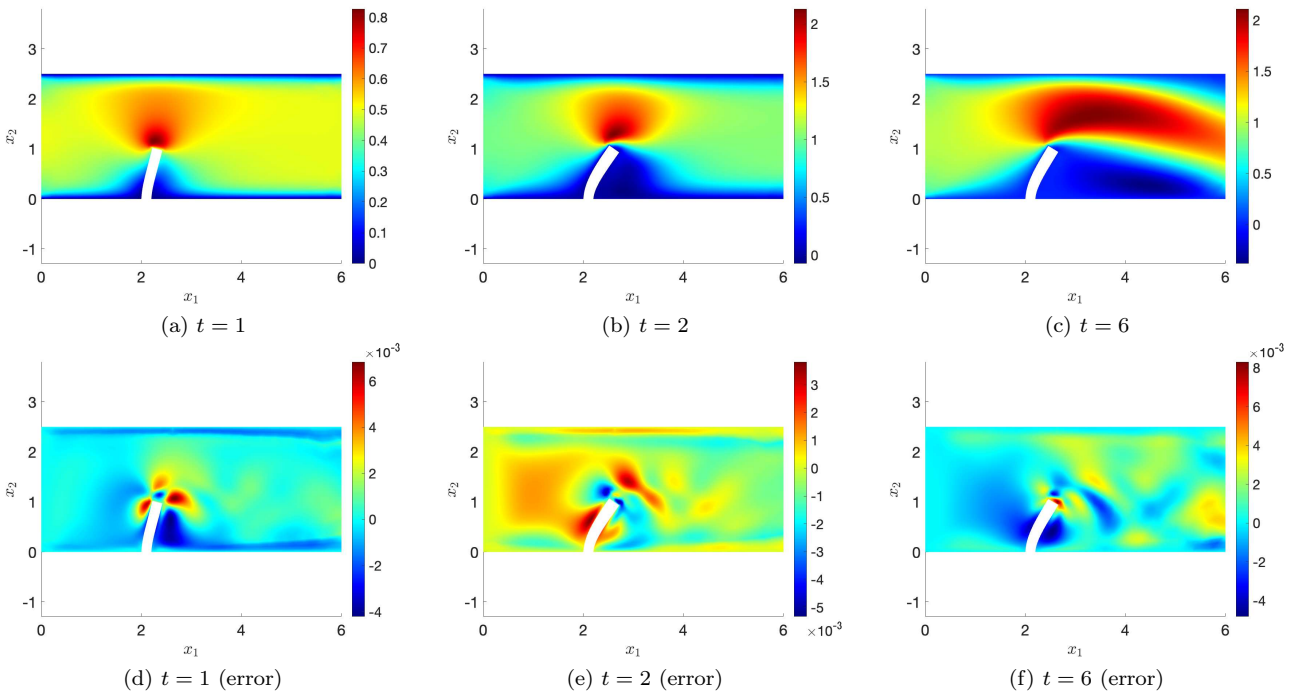


Figure 4: Vertical beam; ROM results obtained using IRK ($s = 2, \Delta t = 0.05$ s, $\text{tol}_{\text{POD}} = 10^{-5}$).

Figure 5 reports the $H^1 \times L^2$ relative error of the velocity-pressure pair as a function of tol_{POD} , together with the corresponding number of reduced modes. As expected, tighter tolerances lead to smaller errors at the price of larger reduced spaces.

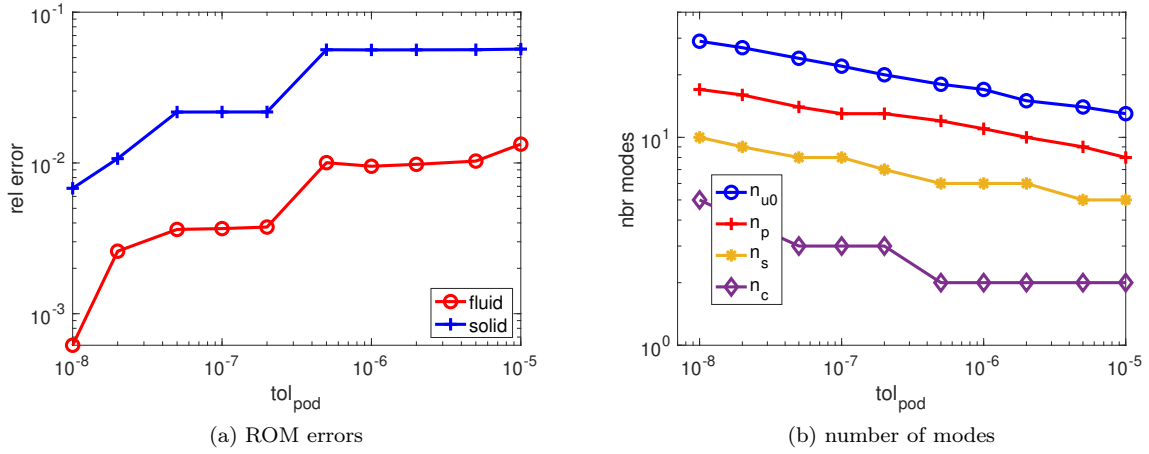


Figure 5: Vertical beam; ROM errors and number of modes in terms of POD tolerance ($s = 2, \Delta t = 0.05$ s).

In Figure 6, we compare high-fidelity and ROM predictions for drag, lift, and tip x -displacement for two representative ROMs built with $\text{tol}_{\text{POD}} = 10^{-6}$ and 10^{-5} . Both ROMs accurately reproduce the force signals and the x -displacement.

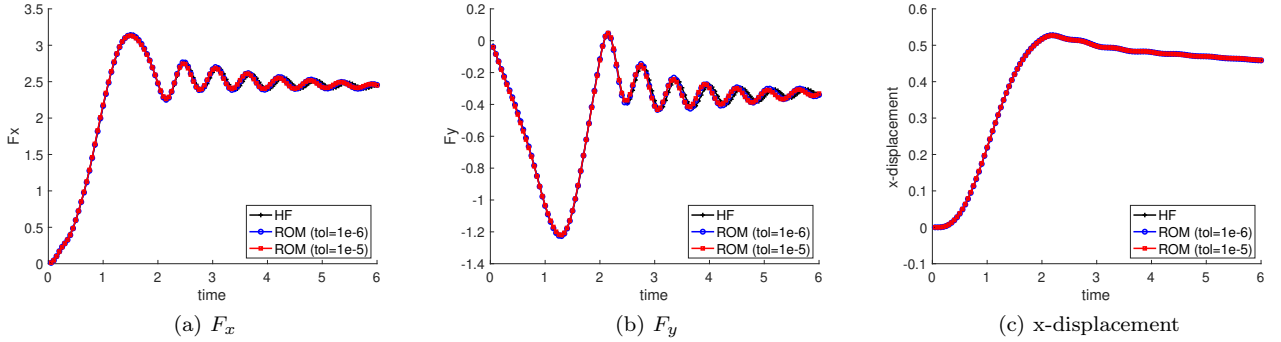


Figure 6: Vertical beam; comparison between HF and two ROM results ($s = 2, \Delta t = 0.05$ s).

We also repeat the ROM analysis for IRK with $s = 3$ and $\Delta t = 0.1$ s. The corresponding velocity fields, error plots, and error versus tolerance curves confirm the same qualitative behavior observed for $s = 2$: ROMs remain stable and accurate, and the use of larger POD tolerances reduces the number of retained POD modes at the cost of increased approximation errors. These additional results are reported in B.1.

Parametric case. We consider the Young's modulus E_s and the mass ratio $m^* := \frac{\rho_s}{\rho_f}$ as parameters, with ranges $E_s/10^3 \in [1, 10]$ and $m^* \in [0.5, 2]$, while keeping ρ_f fixed. We consider $s = 2$ stages and time step $\Delta t = 0.05$ for the IRK time integrator. To build and assess the ROM, we generate 20 training points and 5 additional test points. In Figure 7, we show predictions of the lift and drag forces, as well as the beam tip displacement in the x -direction, obtained using two different ROM tolerances. The predictions demonstrate good accuracy and robustness of the reduced-order model across the considered parametric ranges.

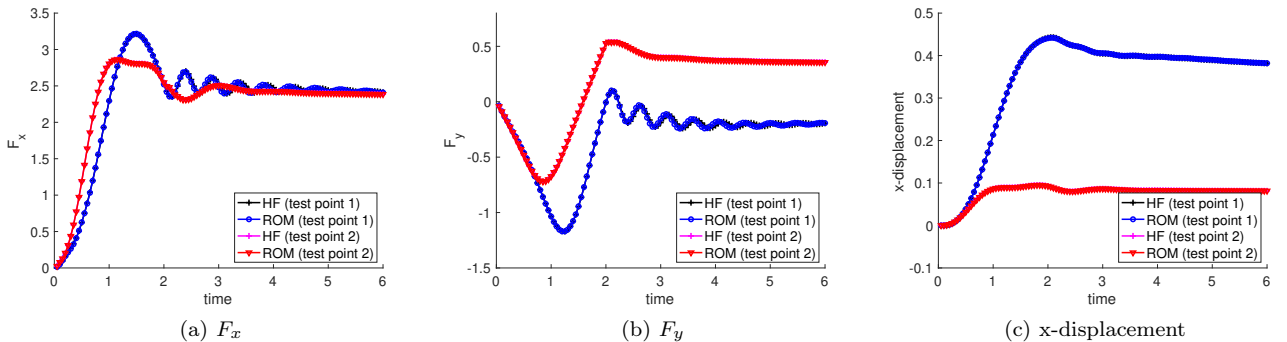


Figure 7: Vertical beam; drag and lift forces, and tip x -displacement at two representative test points.

5.2 Turek

We now consider the widely-used Turek FSI3 benchmark [66], which consists of an incompressible flow past a cylinder with an attached elastic beam. The cylinder is rigid and stationary, and the elastic beam is fixed at its left edge (attached to the cylinder) while the remainder is free to deform under fluid-induced forces. We follow the standard geometric configuration and parameter choices described in [66, 49]. We initialize the FSI simulation by first holding the beam fixed in its undeformed configuration for $T_0 = 30$ s to allow the vortex shedding pattern to develop. Then, at $t = T_0$, we release the beam and integrate the coupled FSI system forward in time.

5.2.1 HF results

Figure 8 shows the horizontal velocity field at three time instants $t = 32, 35, 38$ s obtained using the Radau-IIA IRK scheme with $s = 2$ stages (3rd-order accuracy, hereafter referred as IRK3) and time step $\Delta t = 0.01$ s. The plots illustrate the formation of a periodic vortex street downstream of the cylinder and the associated oscillatory motion of the beam.

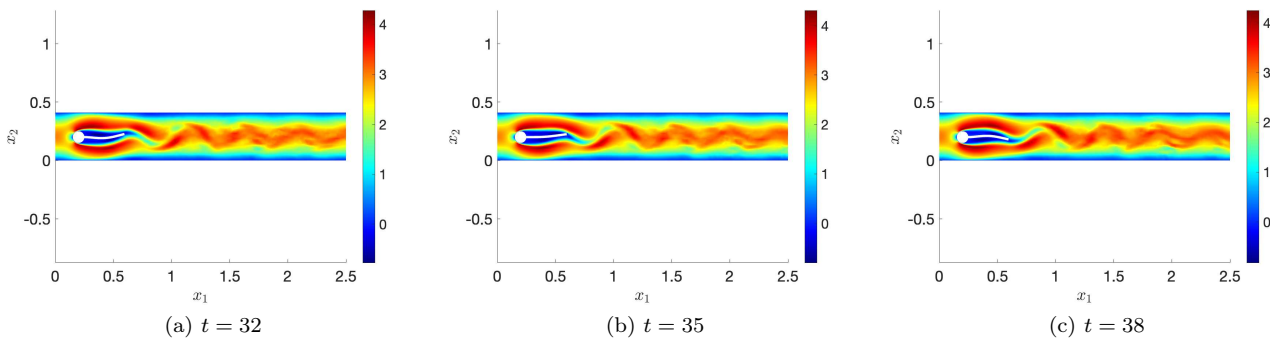


Figure 8: Turek; x-velocity field at 3 time instants.

In Figure 9 we report the long-time histories of the drag and lift forces acting on the cylinder-beam system, together with the total energy for IRK3. After an initial transient, all three signals converge to a periodic regime. The total energy remains bounded and exhibits small periodic variations, which confirms the long-time stability of the IRK discretization.

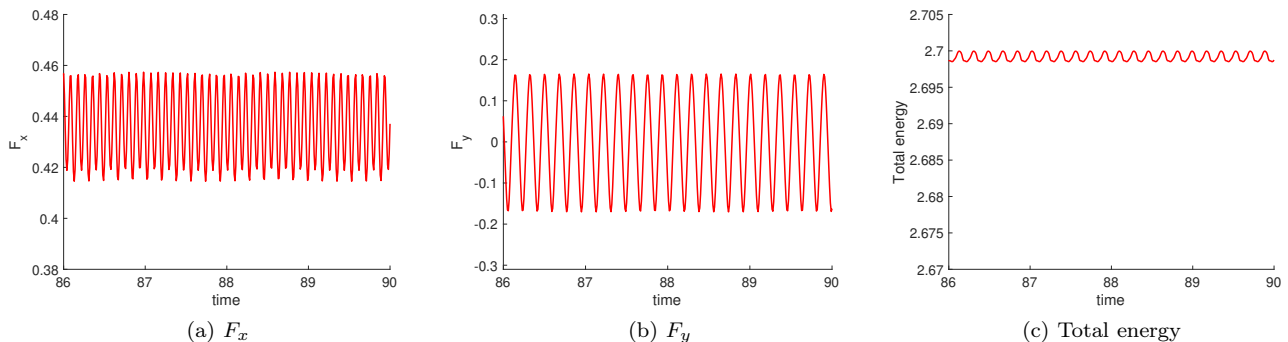


Figure 9: Turek; stable long-time HF results obtained using IRK3.

For comparison, we also consider the time integrator with BDF2 for the fluid and the Newmark scheme ($\beta = \frac{1}{4}$, $\gamma = \frac{1}{2}$) for the solid. The corresponding long time histories of drag, lift, and total energy, shown in Figure 10, reveal an instability: the force amplitudes and the total energy grow in time: this indicates that this time integration pair is not robust in this FSI setting.

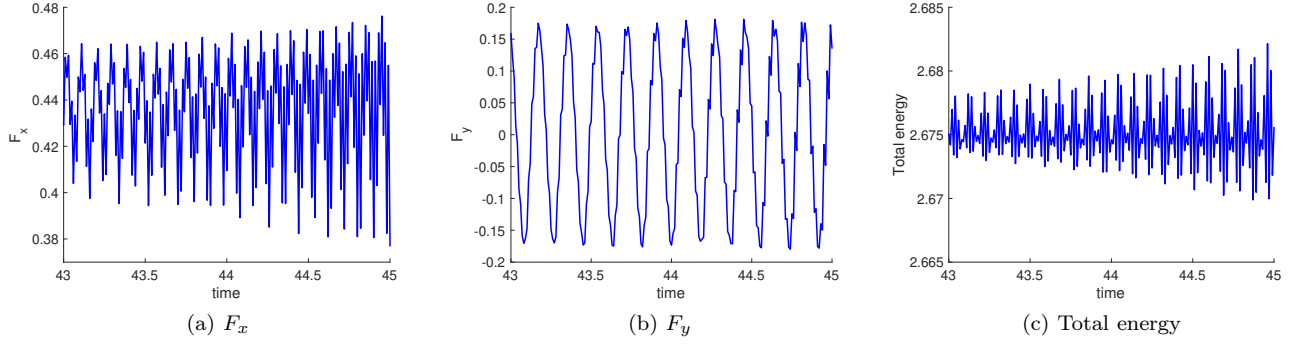


Figure 10: Turek; HF instability using BDF2 + Newmark.

To mitigate this problem, we introduce numerical damping in the Newmark method and choose $\beta = \frac{1}{3}$ and $\gamma = \frac{3}{5}$ ($2\beta \geq \gamma \geq \frac{1}{2}$ to ensure unconditional stability). With these parameters, the instability observed with the undamped Newmark scheme disappears, as shown in Figure 11. Note, however, that the predicted total energy is significantly lower than the one predicted by the IRK scheme: this is consistent with the observation that IRK schemes are less dissipative than damped BDF-Newmark methods.

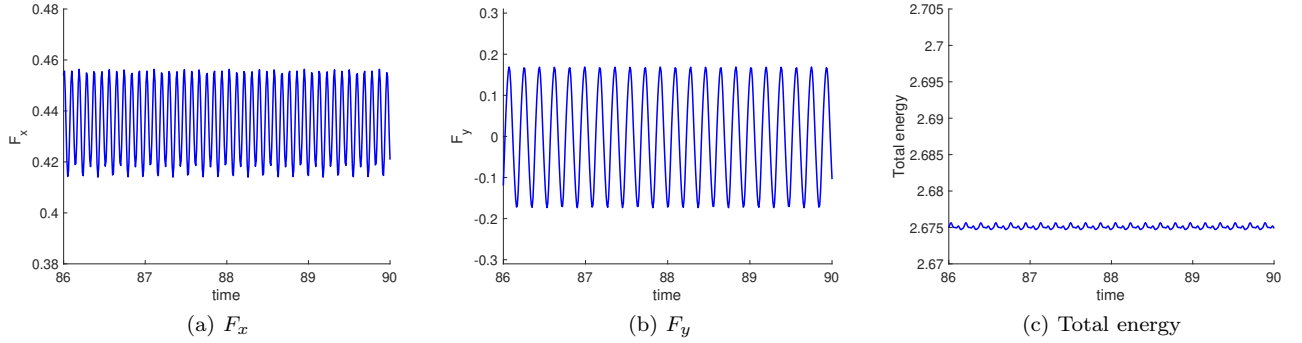


Figure 11: Turek; stable long-time HF results obtained using Newmark method with damping.

We further assess the influence of the IRK order and time step by performing simulations with $s = 2, 3, 4$ and $\Delta t = 0.01, 0.02$ s, and comparing the resulting drag and lift histories. For each fixed time step, the force histories obtained with $s = 2, s = 3, s = 4$ align well. All runs remain stable over the considered time interval, and the differences in amplitude and phase are very small. The corresponding time histories are reported in B.2. We further quantify these observations in the frequency domain. Figure 12 shows the single-sided amplitude spectra of the drag (F_x) and lift (F_y) forces for six runs:

(1) $s = 2, \Delta t = 0.01$; (2) $s = 3, \Delta t = 0.01$; (3) $s = 4, \Delta t = 0.01$; (4) $s = 2, \Delta t = 0.02$; (5) $s = 3, \Delta t = 0.02$; (6) $s = 4, \Delta t = 0.02$. The dominant frequency and the overall spectral shape are essentially identical across all runs. Table 2 summarizes the drag (F_x) and lift (F_y) amplitudes (mean \pm half peak-to-peak) for all six runs and confirms the robustness of the IRK schemes with respect to s and Δt .

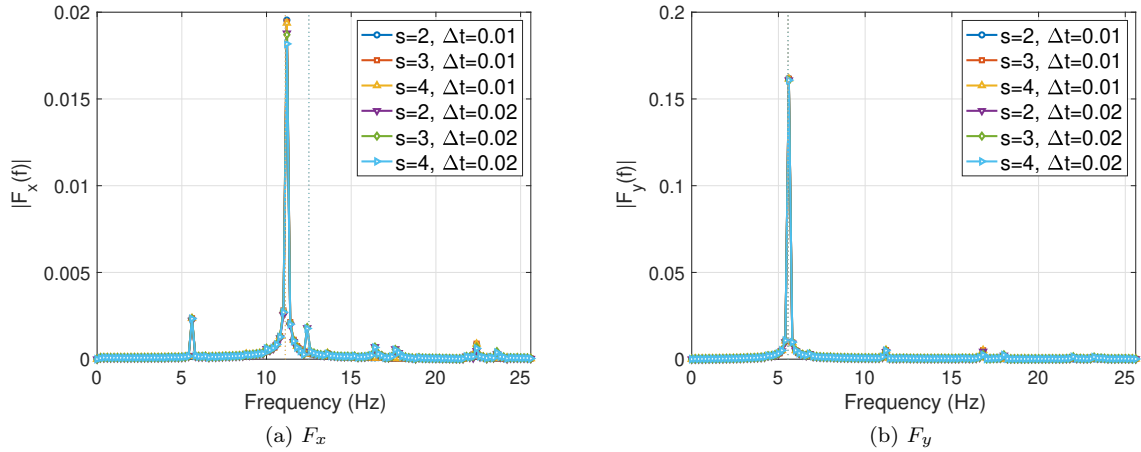


Figure 12: Turek; comparison of spectrum for 6 runs.

Table 2: Drag (F_x) and lift (F_y) amplitudes for the six runs (reported as mean \pm half peak-to-peak).

Run	s	Δt	F_x amplitude	F_y amplitude
1	2	0.01	0.436 ± 0.0198	0.0029 ± 0.1668
2	3	0.01	0.436 ± 0.0198	0.0029 ± 0.1676
3	4	0.01	0.436 ± 0.0197	0.0029 ± 0.1676
4	2	0.02	0.436 ± 0.0190	0.0026 ± 0.1619
5	3	0.02	0.436 ± 0.0190	0.0030 ± 0.1647
6	4	0.02	0.436 ± 0.0184	0.0030 ± 0.1646

5.2.2 ROM results

We next build ROMs from IRK snapshots and assess their performance. We train with snapshots from time instants $t = 30 - 33$ s, then we perform ROM calculation for $t = 30 - 39$ s. We first consider $s = 2, \Delta t = 0.01$ s for the time integrator. We show the horizontal velocity field computed by the ROM at $t = 32, 35, 38$ s for a POD tolerance $\text{tol}_{\text{POD}} = 10^{-6}$ in Figure 13. The errors remain small compared to the magnitude of the flow, which indicates that the ROM correctly reproduces the main flow features and the beam motion.

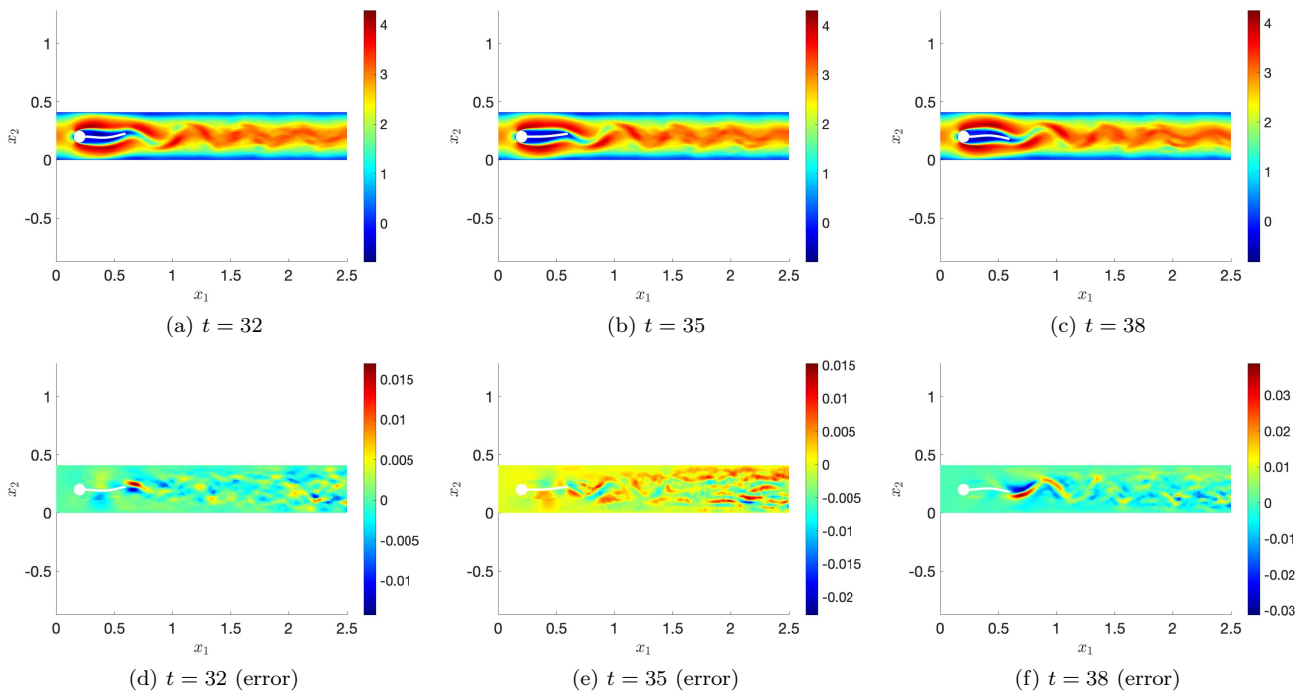


Figure 13: Turek; stable ROM results obtained using IRK ($s = 2, \Delta t = 0.01$ s).

We show $H^1 \times L^2$ relative error of the velocity-pressure pair as function of the POD tolerance, together with the corresponding number of reduced modes in Figure 14. As expected, the use of tighter tolerances tol_{POD} leads to smaller errors but larger reduced spaces. The fluid velocity basis is enriched with supremizer modes to ensure the inf-sup stability, and thus the total number of velocity modes for the fluid is $n_u = n_{u0} + n_p$.

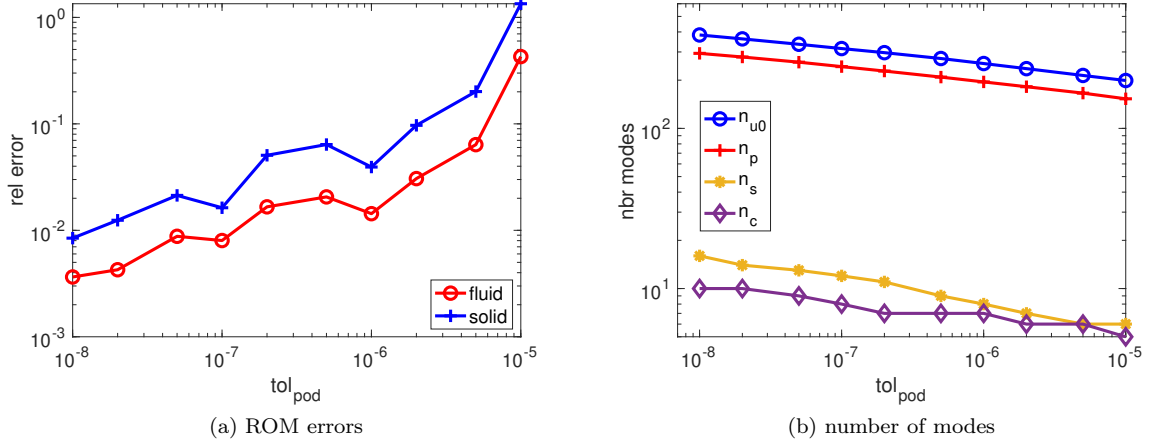


Figure 14: Turek; ROM errors and number of modes in terms of POD tolerance ($s = 2, \Delta t = 0.01$ s).

In Figure 15, we compare high-fidelity and ROM predictions for drag, lift, and total energy for two representative ROMs built with $\text{tol}_{\text{POD}} = 10^{-7}$ and 10^{-6} . Both ROMs can reproduce the force signals and total energy; the ROM with the smaller tolerance provides a slightly better phase match.

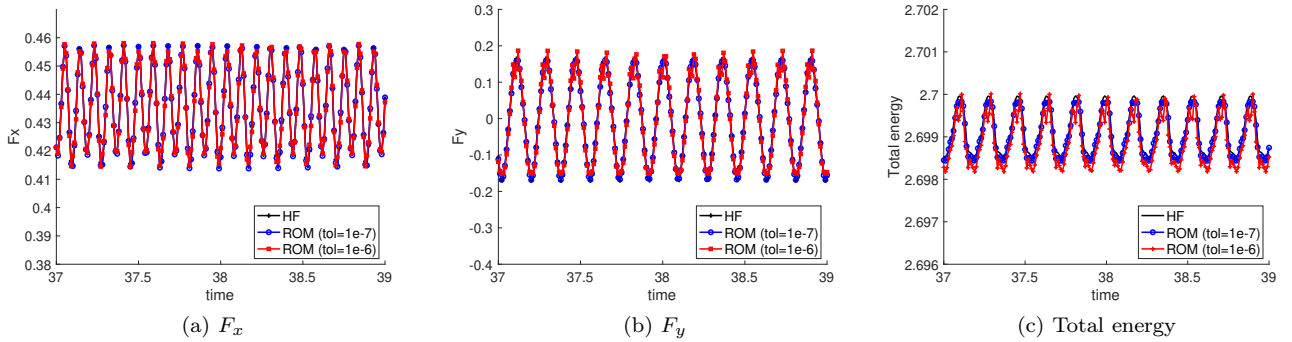


Figure 15: Turek; comparison between HF and two ROM results ($s = 2, \Delta t = 0.01$ s).

We also repeat the analysis for IRK with $s = 3$ and $\Delta t = 0.02$ s. The corresponding velocity fields, error plots, and error versus tolerance curves confirm the same qualitative behavior: ROMs remain stable and accurate, and the dimension accuracy trade-off with respect to tol_{POD} is similar to the $s = 2$ case. These additional results are reported in B.3. Figure 16 shows the single-sided amplitude spectra of the drag (F_x) and lift (F_y) forces computed by the ROMs for different numbers of IRK stages s , time steps Δt , and POD tolerances tol_{POD} . All ROM spectra closely match the dominant frequency and overall spectral distribution of the high-fidelity reference, indicating that the proposed ROM framework accurately captures the frequency content of fluid forces over a range of numerical settings.

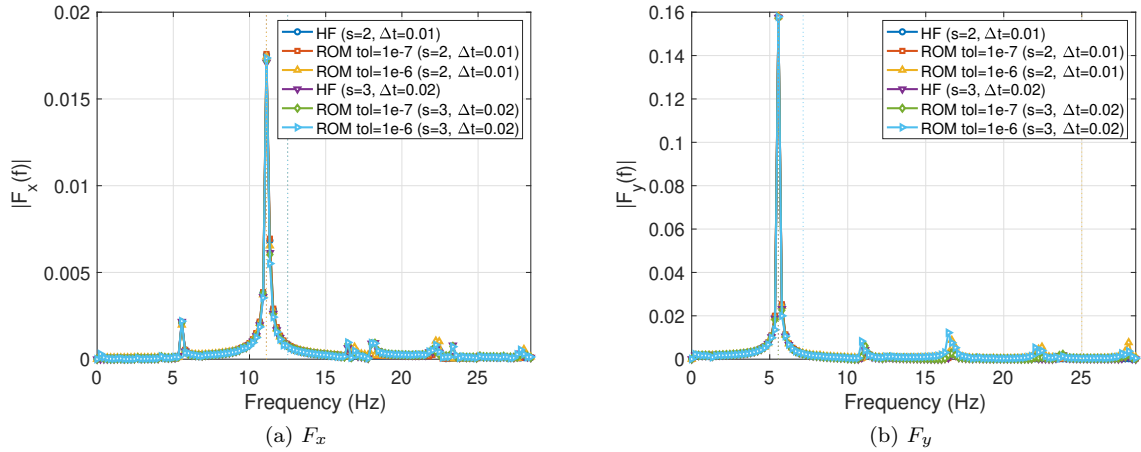


Figure 16: Turek; spectra of drag and lift forces obtained by ROMs for different s , Δt , and tol_{POD} .

A key advantage of the present method with respect to the flux-based strategy of [49] is its long time robustness at the reduced level. To illustrate this, we construct a POD basis from IRK snapshots ($s = 2$) with $\text{tol}_{\text{POD}} = 2 \times 10^{-7}$ and compare the effect of advancing this basis in time with different time integrators. When the ROM is integrated with IRK ($s = 2$), the solution remains stable and accurately follows the high-fidelity reference. In contrast, the use of the BDF2-Newmark scheme for time integration renders the ROM unstable, irrespective of numerical (Newmark) damping. This behaviour is illustrated in Figure 17 for the drag and lift forces.

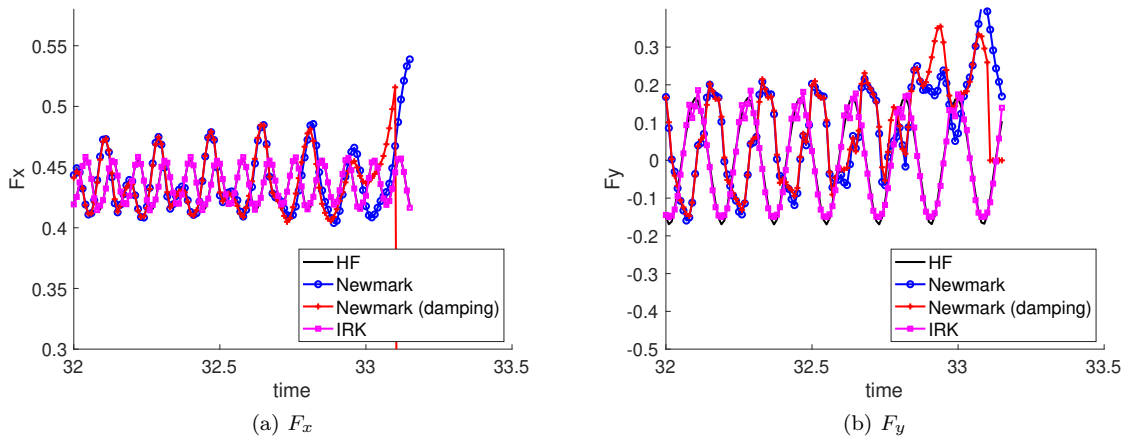


Figure 17: Turek; comparison between BDF2 + Newmark and IRK ROM results ($s = 2$, $\Delta t = 0.01$ s, $\text{tol}_{\text{POD}} = 2 \cdot 10^{-7}$).

We also investigate ROMs trained on periodic snapshots only. In this case, we use snapshots from time instants $t = 33 - 35$ s, as training set. The snapshots are in a fully developed periodic regime. We then perform the ROM calculation for $T = 33 - 39$ s. Figure 18 shows the $H^1 \times L^2$ relative error of the velocity–pressure pair and the number of reduced modes as functions of tol_{POD} .

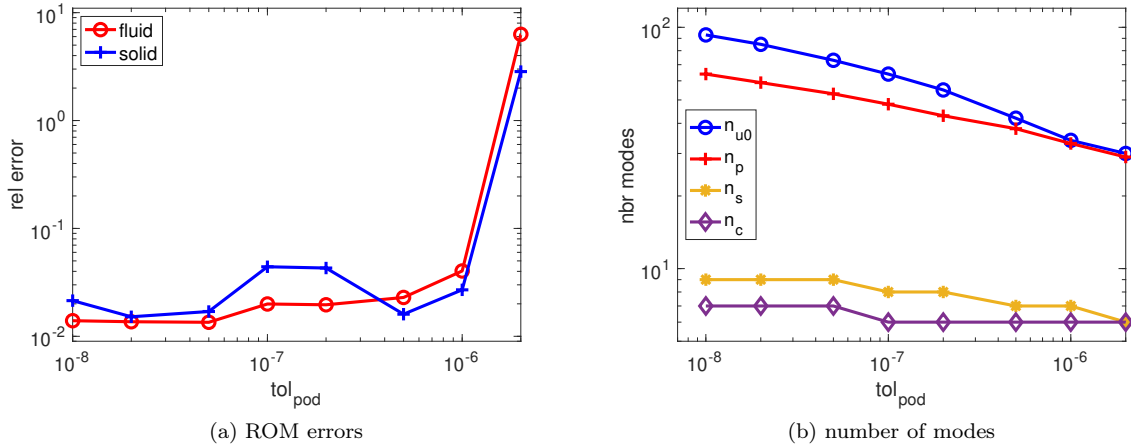
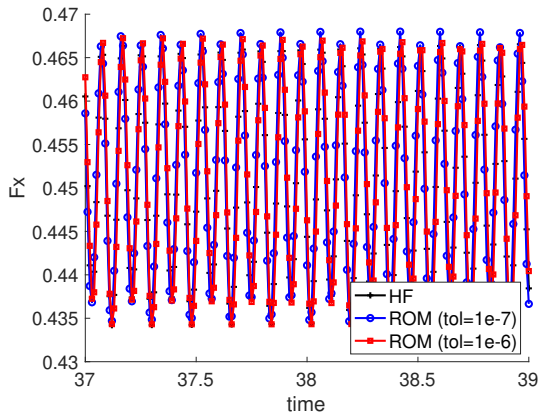
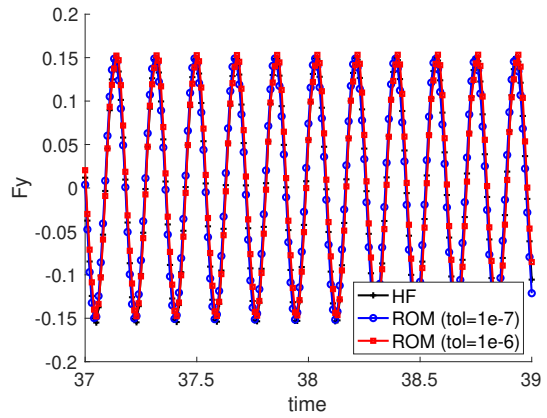


Figure 18: Turek; ROM errors and number of modes in terms of POD tolerance using periodic snapshots ($s = 2, \Delta t = 0.01$ s).

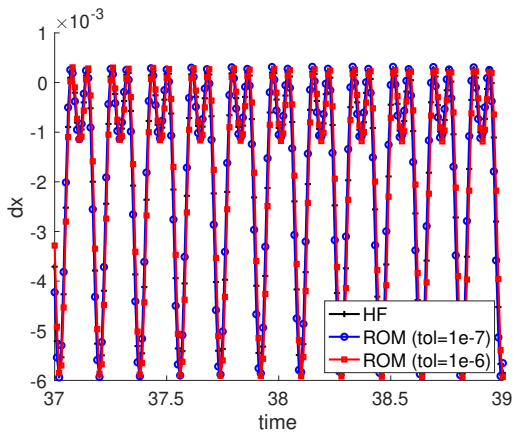
Parametric case. Finally, we perform a parametric study in which we vary the fluid viscosity $\mu_f \in [0.75, 1.3]$ and the mass ratio $m^* := \frac{\tilde{\rho}_s}{\rho_f} \in [0.5, 2]$, while keeping ρ_f fixed. We consider $s = 2, \Delta t = 0.01$ s for the IRK time integrator. We randomly generate 20 training points and 5 test points. For each training parameter, we collect HF snapshots over the time window $I_{\text{train}} = [33, 36]$ [s], which are used to construct the reduced basis. The resulting ROMs are then run and subsequently assessed over the extended time interval $I_{\text{test}} = [33, 39]$ s. Figures 19 and 20 compare the high-fidelity and ROM predictions at two representative test points. In both cases, the ROM solutions remain stable, and accurately reproduce the amplitude of the drag and lift forces, as well as the horizontal and vertical displacements of a probe point on the beam. Figure 21 shows the single-sided amplitude spectra of the drag (F_x) and lift (F_y) forces computed by ROMs at two representative test points. The two points exhibit different dominant frequencies, and the ROMs consistently capture the dominant frequency and the overall spectral characteristics across the considered POD tolerances. These results demonstrate the robustness and predictive capability of the ROM in the parametric regime. Figure 22 reports the number of POD modes required to achieve a given tolerance in the parametric setting. We observe that the parametric dependence significantly increases the number of POD modes that are required to meet the target accuracy: this clearly deteriorates the efficiency of the linear-subspace ROM and ultimately motivates the development of nonlinear model reduction strategies to further enhance computational efficiency in parametric FSI problems.



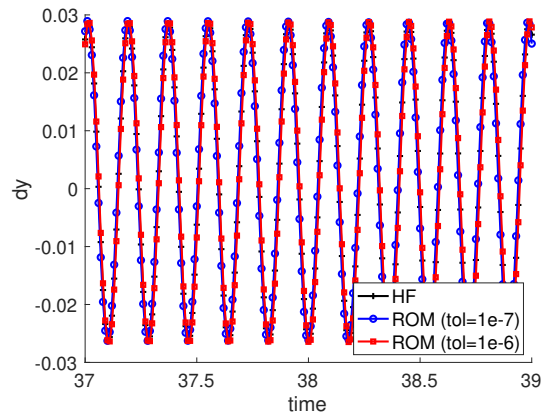
(a) F_x



(b) F_y



(c) d_x



(d) d_y

Figure 19: Turek; comparison between HF and two ROM results (test point 1).

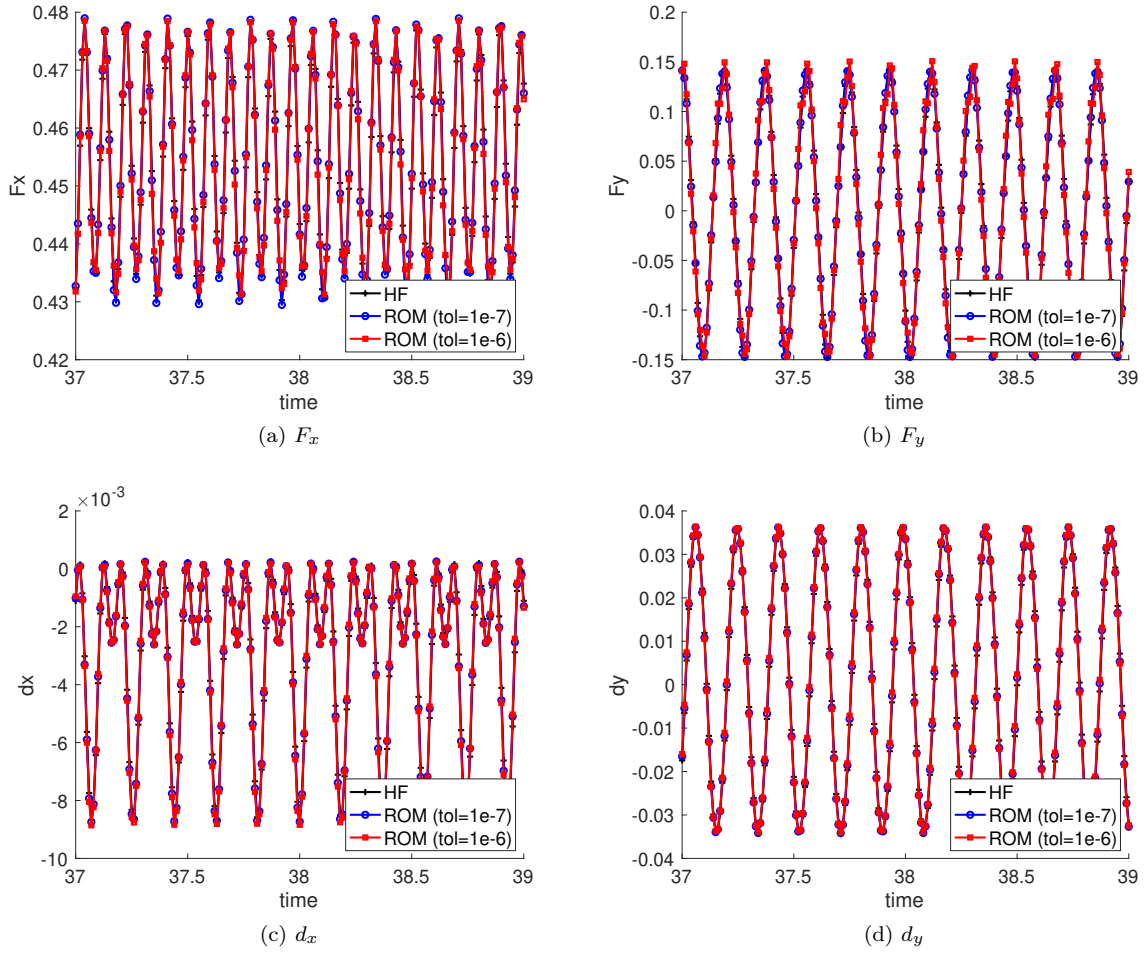


Figure 20: Turek; comparison between HF and two ROM results (test point 2).

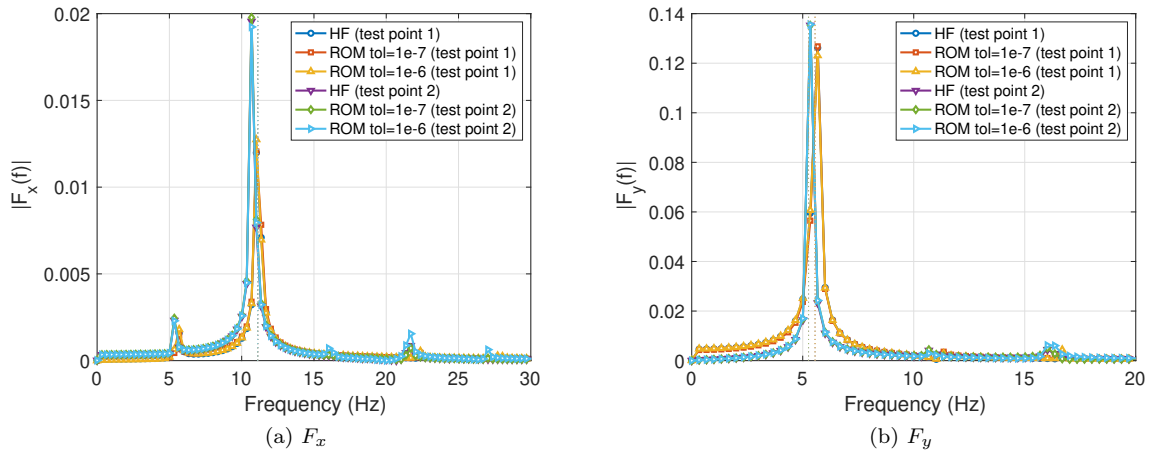


Figure 21: Turek; comparison of spectra of drag and lifted forces obtained by ROMs for different tol_{POD} at two representative test points.

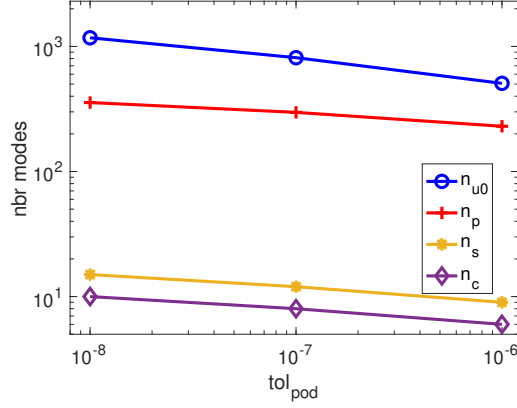


Figure 22: Turek; number of modes in terms of POD tolerance in the parametric case.

6 Conclusion

In this paper, we introduced a new component-based model order reduction method for incompressible fluid-structure interaction (FSI) problems, that leverages implicit Runge-Kutta (IRK) schemes and a displacement-based interface control strategy. We rigorously verified the semi-discrete energy balance properties at the reduced-order level. Numerical experiments demonstrated that the combination of high-order Radau-IIA IRK schemes with the displacement-based interface coupling significantly improves the numerical stability of the reduced-order model, and ultimately enables accurate and stable predictions of the long-time response.

For future research, we plan to extend the current framework toward fully energy-conserving numerical schemes at both the full-order and reduced-order levels. Second, we plan to combine our formulation with nonlinear approximation techniques to mitigate the issue of the slow decay of the Kolmogorov n -width. Third, we plan to apply our formulation to larger-scale systems with many fluid and solid components: towards this end, we plan to investigate localized training strategies to avoid simulations of the full system and also effective hyper-reduction techniques to speed up online calculations.

A Alternative derivation of the fully discrete FSI formulation

For completeness, we present an equivalent derivation of (17) obtained by first applying the IRK scheme to the uncoupled fluid and solid semi-discrete equations and then assembling the coupled stage system using the mask matrices as in (10).

The fluid subsystem is represented by the differential-algebraic equation (DAE):

$$\begin{cases} \frac{d\mathbf{M}_f \mathbf{u}_f}{dt} + \mathbf{R}'_f(t, \mathbf{u}_f, \mathbf{p}_f, \mathbf{P}_{s,\Gamma} \mathbf{d}_s) = 0, \\ \mathbf{B}_f(\mathbf{P}_{s,\Gamma} \mathbf{d}_s) \mathbf{u}_f = 0. \end{cases} \quad (31)$$

Here, the solid displacement \mathbf{d}_s (and ALE mesh velocity) are treated as prescribed at the IRK stages. Applying the IRK scheme [67] yields, for each stage $i = 1, \dots, s$,

$$\begin{cases} \mathbf{R}_f^{(n+c_i)} = 0, \\ \mathbf{B}_f^{(n+c_i)} \mathbf{u}_f^{(n+c_i)} = 0, \end{cases} \quad (32)$$

where the fully discrete fluid stage residual

$$\mathbf{R}_f^{(n+c_i)} := \mathbf{M}_f^{(n+c_i)} \mathbf{u}_f^{(n+c_i)} - \mathbf{M}_f^{(n)} \mathbf{u}_f^{(n)} + \Delta t \sum_{j=1}^s a_{ij} \mathbf{R}'_f \left(t^{(n+c_j)}, \mathbf{u}_f^{(n+c_j)}, \mathbf{p}_f^{(n+c_j)}, \mathbf{d}_s^{(n+c_j)} \right).$$

For the solid, we transform the second-order equation into a first-order system by introducing the velocity variable $\mathbf{u}_s = \dot{\mathbf{d}}_s$, obtaining the ODEs:

$$\begin{cases} \frac{d\mathbf{M}_s \mathbf{u}_s}{dt} + \mathbf{R}'_s(t, \mathbf{d}_s) = 0, \\ \dot{\mathbf{d}}_s = \mathbf{u}_s. \end{cases} \quad (33)$$

The IRK discretization reads

$$\begin{cases} \mathbf{R}_s^{(n+c_i)} = 0, \\ \mathbf{d}_s^{(n+c_i)} - \mathbf{d}_s^{(n)} - \Delta t \sum_{j=1}^s a_{ij} \mathbf{u}_s^{(n+c_j)} = 0, \end{cases} \quad \text{for } i = 1, \dots, s, \quad (34)$$

where the fully discrete solid stage residual

$$\mathbf{R}_s^{(n+c_i)} := \mathbf{M}_s \mathbf{u}_s^{(n+c_i)} - \mathbf{M}_s \mathbf{u}_s^{(n)} + \Delta t \sum_{j=1}^s a_{ij} \mathbf{R}'_s \left(t^{(n+c_j)}, \mathbf{d}_s^{(n+c_j)} \right).$$

The stage velocities $\mathbf{u}_s^{(n+c_i)}$ in the solid stage residual are then eliminated by substituting the kinematic relation (34)₂ into (34)₁, resulting in a system that involves only the unknown variable $\mathbf{d}_s^{(n+c_i)}$.

By combining fluid and solid residuals defined above, and incorporating interface coupling conditions and boundary conditions through Boolean mask matrices, we obtain the fully discrete coupled FSI system at each IRK stage (17).

B Additional numerical results

B.1 Vertical beam: ROM results for $s = 3$, $\Delta t = 0.1$

We report here the ROM results for IRK with $s = 3$ and $\Delta t = 0.1$ s, complementing the $s = 2$, $\Delta t = 0.05$ s case discussed in the main text. The POD basis is built from IRK snapshots with $t \in [0, 6]$ s, and the ROM is advanced over the same time interval. Figure 23 shows the ROM horizontal velocity field and corresponding pointwise error at $t = 1, 2, 6$ s for $\text{tol}_{\text{POD}} = 10^{-5}$. The ROM remains stable and provides an accurate approximation of the HF solution.

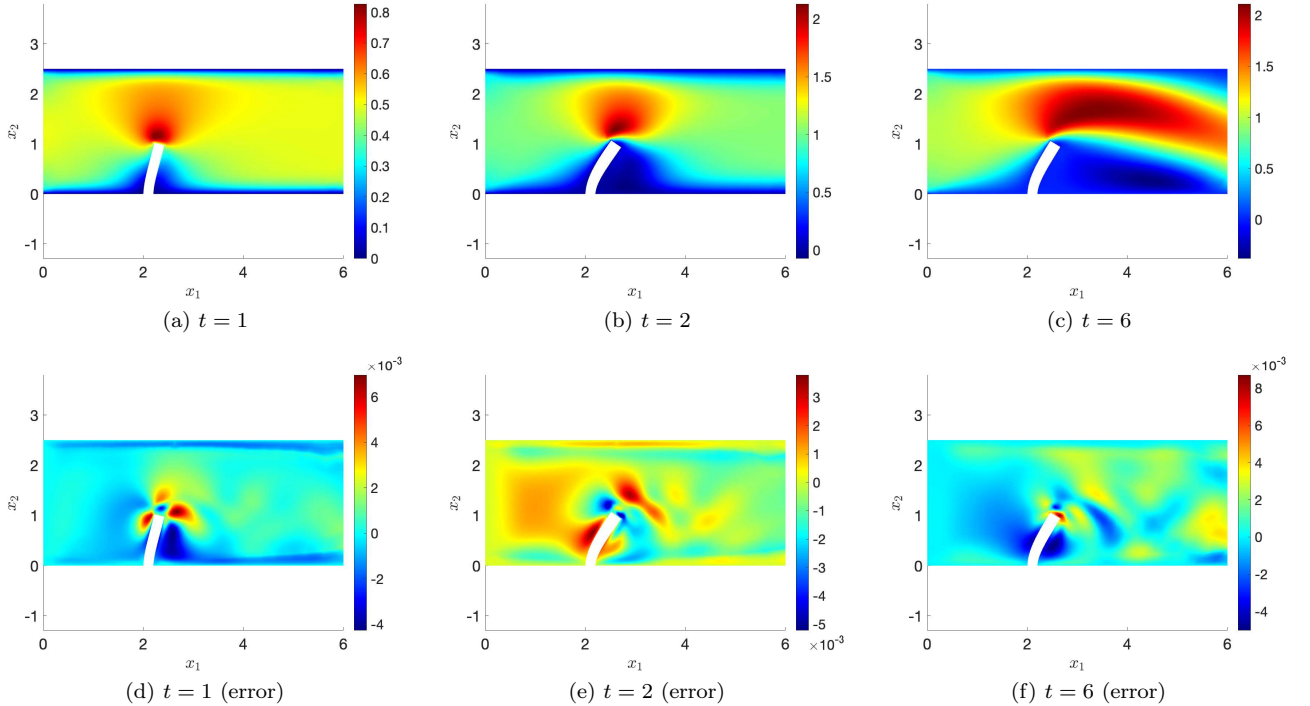


Figure 23: Vertical beam; ROM horizontal velocity and pointwise error for IRK with $s = 3$, $\Delta t = 0.1$ s and $\text{tol}_{\text{POD}} = 10^{-5}$.

Figure 24 shows the $H^1 \times L^2$ relative error of the velocity-pressure pair and the number of modes as functions of tol_{POD} . As in the $s = 2$ case, relaxing the POD tolerance reduces the number of modes but increases the approximation error.

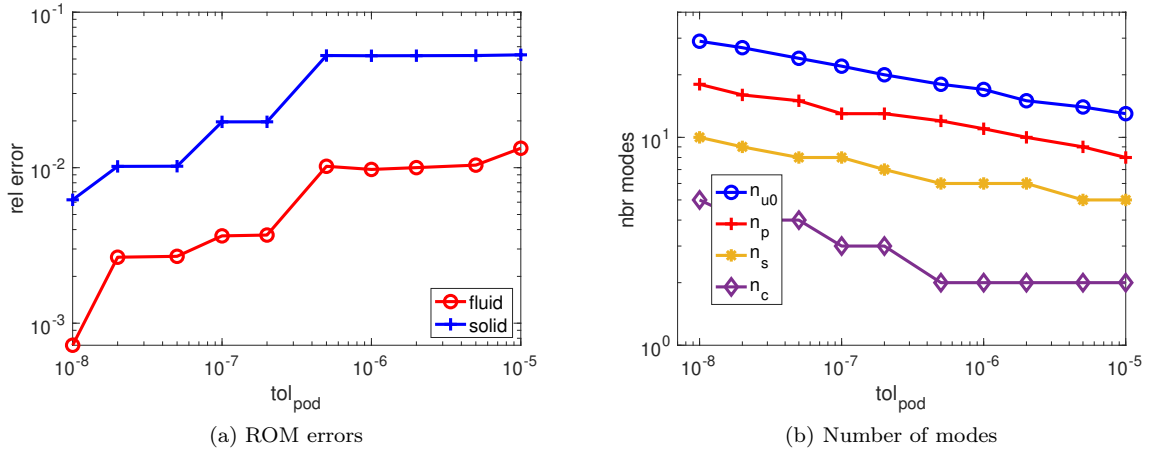


Figure 24: Vertical beam; ROM errors and number of modes versus POD tolerance ($s = 3$, $\Delta t = 0.1$ s).

Figure 25 compares HF and ROM predictions for drag, lift, and tip x -displacement for $\text{tol}_{\text{POD}} = 10^{-6}$ and 10^{-5} . In both cases, the ROMs reproduce the force and displacement histories with good agreement and no sign of instability, confirming the robustness of the IRK-based bubble-port ROM for this test.

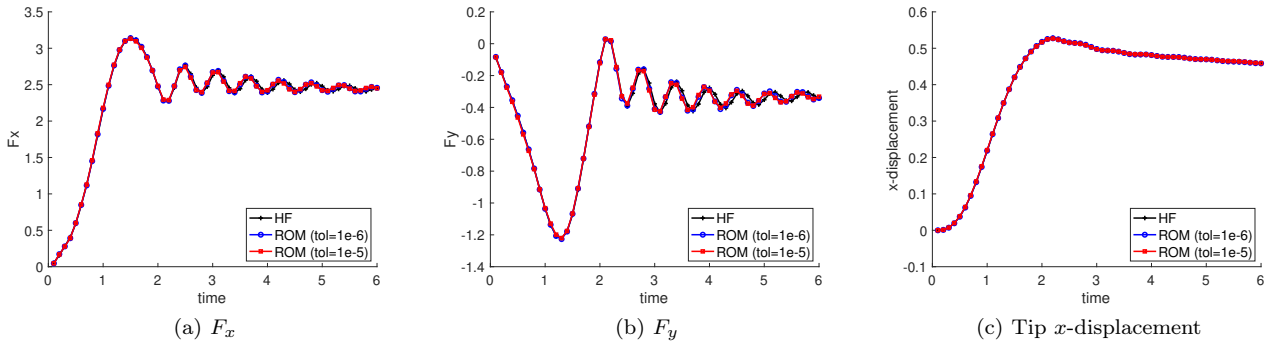


Figure 25: Vertical beam; comparison between HF and ROM predictions for F_x , F_y , and tip x -displacement ($s = 3$, $\Delta t = 0.1$ s).

B.2 Turek: HF results

We examine the influence of the Radau-IIA time integrator on the Turek FSI3 benchmark by varying the number of stages $s = 2, 3, 4$ and the time step $\Delta t = 0.01, 0.02$ s. The corresponding drag and lift histories are shown in Figures 26–27. For both time steps, all three IRK schemes yield almost indistinguishable force signals, with negligible differences in amplitude and phase.

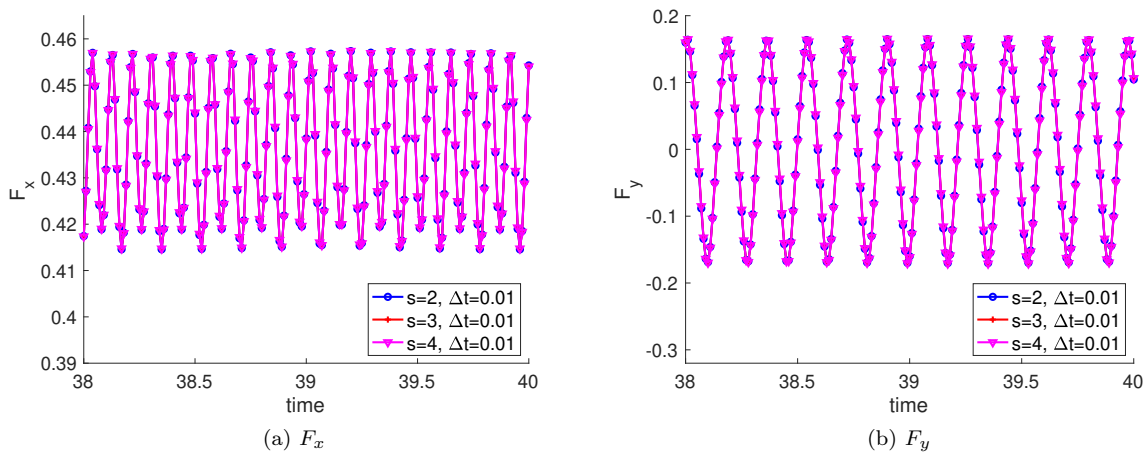


Figure 26: Turek; comparison of drag and lift using $s = 2, 3, 4$ and $\Delta t = 0.01$ s.

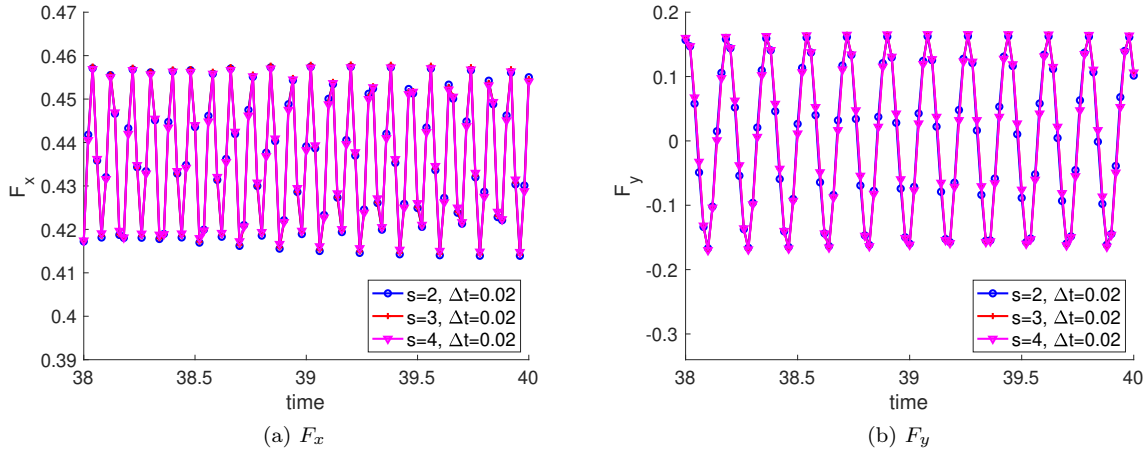


Figure 27: Turek; comparison of drag and lift using $s = 2, 3, 4$ and $\Delta t = 0.02$ s.

B.3 Turek: ROM results for $s = 3$, $\Delta t = 0.02$

We report here the detailed ROM results for the IRK scheme with $s = 3$ and $\Delta t = 0.02$ s, which complement the $s = 2$, $\Delta t = 0.01$ s results shown in the main text. The POD basis is again built from snapshots in the interval $t \in [30, 33]$ s, and the ROM is advanced up to $t = 39$ s. Figure 28 shows the ROM horizontal velocity field and the corresponding pointwise error at $t = 32, 35, 38$ s for $\text{tol}_{\text{POD}} = 10^{-6}$. The ROM remains stable and accurately captures the flow and beam dynamics.

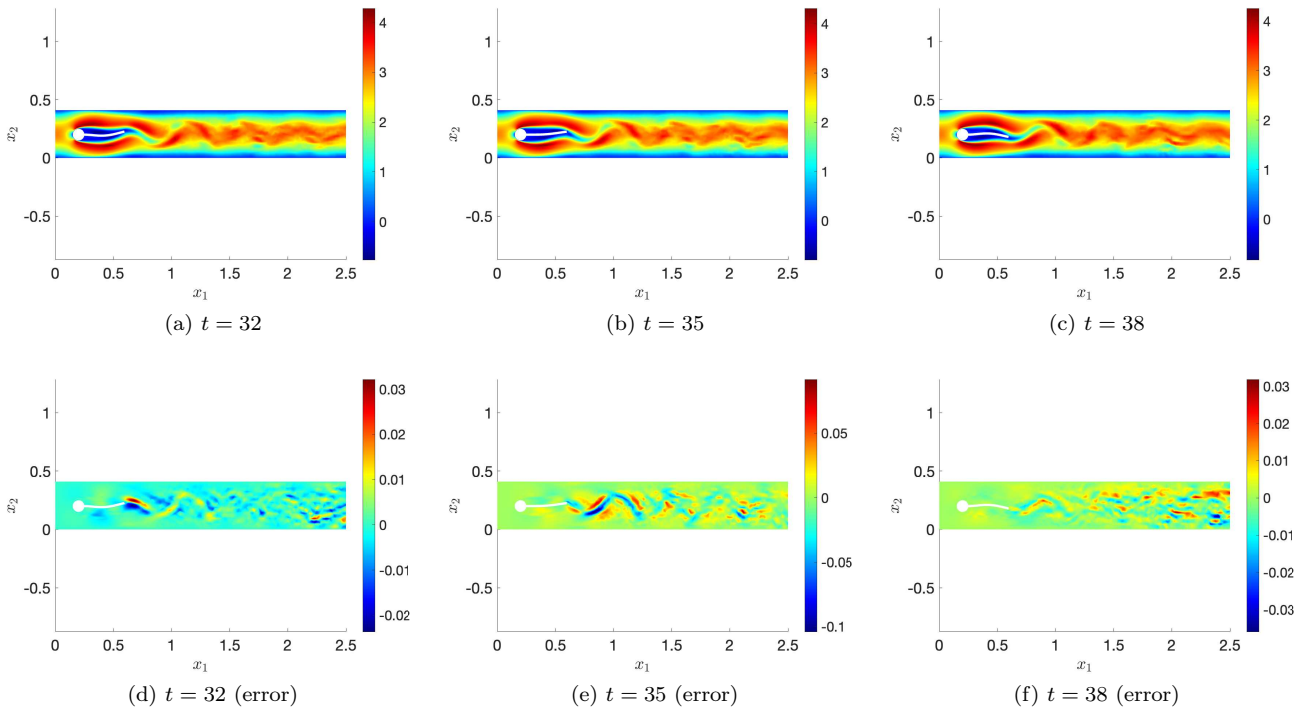


Figure 28: Turek; ROM horizontal velocity and pointwise error for IRK with $s = 3$, $\Delta t = 0.02$ s and $\text{tol}_{\text{POD}} = 10^{-6}$.

Figure 29 shows the $H^1 \times L^2$ relative error of the velocity-pressure pair versus POD tolerance, together with the corresponding number of reduced modes. The behavior is analogous to the $s = 2$ case: smaller tolerances improve accuracy at the cost of larger reduced spaces.

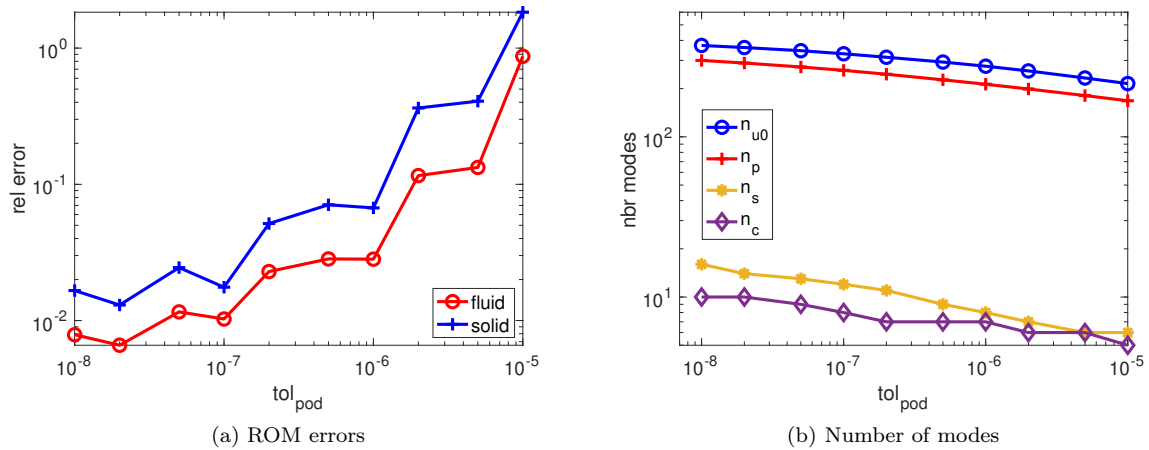


Figure 29: Turek; ROM errors and number of modes versus POD tolerance ($s = 3$, $\Delta t = 0.02$ s).

In Figure 30, we compare HF and ROM predictions for drag, lift, and total energy for two ROMs with $\text{tol}_{\text{POD}} = 10^{-7}$ and 10^{-6} . As in the $s = 2$ case, both ROMs reproduce the force signals and energy evolution with very good agreement and no signs of instability.

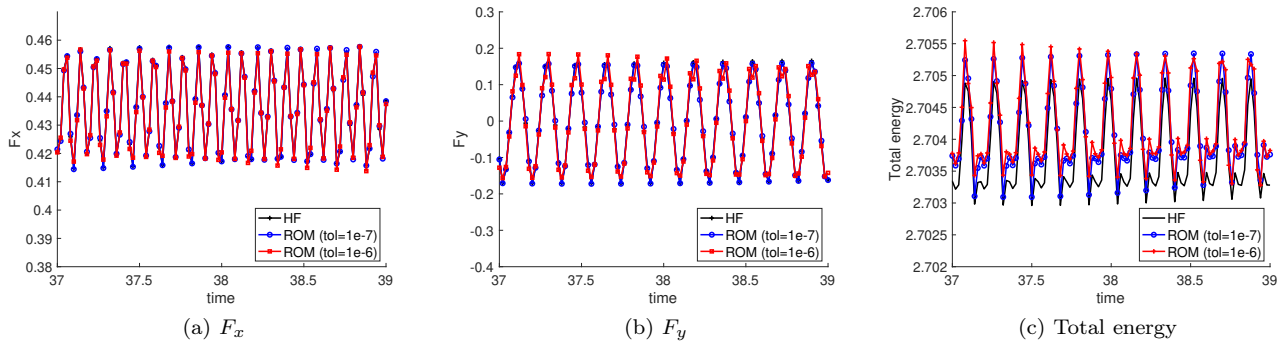


Figure 30: Turek; comparison between HF and ROM results for F_x , F_y , and total energy ($s = 3$, $\Delta t = 0.02$ s).

References

- [1] S. Piperno, C. Farhat, B. Larrouturou, Partitioned procedures for the transient solution of coupled aeroelastic problems part I: Model problem, theory and two-dimensional application, *Computer methods in applied mechanics and engineering* 124 (1-2) (1995) 79–112.
- [2] S. Piperno, C. Farhat, Partitioned procedures for the transient solution of coupled aeroelastic problems—part II: energy transfer analysis and three-dimensional applications, *Computer methods in applied mechanics and engineering* 190 (24-25) (2001) 3147–3170.
- [3] L. Wang, R. Quant, A. Kolios, Fluid structure interaction modelling of horizontal-axis wind turbine blades based on CFD and FEA, *Journal of Wind Engineering and Industrial Aerodynamics* 158 (2016) 11–25.
- [4] B. Battisti, G. Bracco, M. Bergmann, A multi-fidelity model for wave energy converters, *International Journal for Numerical Methods in Fluids* 97 (4) (2025) 427–445.
- [5] E. B. Agamloh, A. K. Wallace, A. Von Jouanne, Application of fluid–structure interaction simulation of an ocean wave energy extraction device, *Renewable Energy* 33 (4) (2008) 748–757.
- [6] P. Crosetto, S. Deparis, G. Fourestey, A. Quarteroni, Parallel algorithms for fluid-structure interaction problems in haemodynamics, *SIAM Journal on Scientific Computing* 33 (4) (2011) 1598–1622.
- [7] P. Sun, C.-S. Zhang, R. Lan, L. Li, An advanced ALE-mixed finite element method for a cardiovascular fluid–structure interaction problem with multiple moving interfaces, *Journal of Computational Science* 50 (2021) 101300.

- [8] V. Ostasevicius, R. Dauksevicius, R. Gaidys, A. Palevicius, Numerical analysis of fluid–structure interaction effects on vibrations of cantilever microstructure, *Journal of Sound and Vibration* 308 (3-5) (2007) 660–673.
- [9] S. Dutta, C. Jog, Monolithic finite element modeling of compressible fluid-structure-electrostatics interactions in MEMS devices, *International Journal for Numerical Methods in Fluids* 96 (12) (2024) 2006–2050.
- [10] A. Quarteroni, A. Manzoni, F. Negri, *Reduced basis methods for partial differential equations: an introduction*, Springer, 2015.
- [11] J. S. Hesthaven, G. Rozza, B. Stamm, *Certified reduced basis methods for parametrized partial differential equations*, Springer, 2016.
- [12] A. Buhr, L. Iapichino, M. Ohlberger, S. Rave, F. Schindler, K. Smetana, Localized model reduction for parameterized problems, in: *Handbook on Model Order Reduction*, Walter De Gruyter, 2020.
- [13] D. B. P. Huynh, D. J. Knezevic, A. T. Patera, A static condensation reduced basis element method: approximation and a posteriori error estimation, *ESAIM: Mathematical Modelling and Numerical Analysis* 47 (1) (2013) 213–251.
- [14] L. Pegolotti, M. R. Pfaller, A. L. Marsden, S. Deparis, Model order reduction of flow based on a modular geometrical approximation of blood vessels, *Computer Methods in Applied Mechanics and Engineering* 380 (2021) 113762. doi:10.1016/j.cma.2021.113762.
- [15] F. Ballarin, G. Rozza, POD–Galerkin monolithic reduced order models for parametrized fluid-structure interaction problems, *International Journal for Numerical Methods in Fluids* 82 (12) (2016) 1010–1034. doi:10.1002/flid.4252.
- [16] F. Ballarin, G. Rozza, Y. Maday, Reduced-order semi-implicit schemes for fluid-structure interaction problems, in: P. Benner, M. Ohlberger, A. Patera, G. Rozza, K. Urban (eds) *Model Reduction of Parametrized Systems. MS&A*, vol 17, Springer, Cham., 2017. doi:https://doi.org/10.1007/978-3-319-58786-8_10.
- [17] M. Nonino, F. Ballarin, G. Rozza, Y. Maday, Projection based semi-implicit partitioned reduced basis method for fluid-structure interaction problems, *Journal of Scientific Computing* 94 (1) (2023) 4. doi:10.1007/s10915-022-02049-6.
- [18] Q. Zhai, S. Zhang, P. Sun, X. Xie, A projection-based time-segmented reduced order model for fluid-structure interactions, *Journal of Computational Physics* 520 (2025) 113481.
- [19] D. Xiao, P. Yang, F. Fang, J. Xiang, C. C. Pain, I. M. Navon, Non-intrusive reduced order modelling of fluid–structure interactions, *Computer Methods in Applied Mechanics and Engineering* 303 (2016) 35–54.
- [20] V. N. Ngan, G. Stabile, A. Mola, G. Rozza, A reduced-order model for segregated fluid–structure interaction solvers based on an ALE approach, *Computers & Fluids* (2025) 106824.
- [21] C. M. Colciago, S. Deparis, Reduced numerical approximation of reduced fluid-structure interaction problems with applications in hemodynamics, *Frontiers in Applied Mathematics and Statistics* 4 (2018) 18.
- [22] S. Deparis, A. Iubatti, L. Pegolotti, Coupling non-conforming discretizations of PDEs by spectral approximation of the Lagrange multiplier space, *ESAIM: Mathematical Modelling and Numerical Analysis* 53 (5) (2019) 1667–1694.
- [23] C. M. Colciago, D. Forti, S. Deparis, Fluid–structure interaction for vascular flows: from supercomputers to laptops, *Fluid–structure interaction. Modeling, adaptive discretisations and solvers*, *Radon Series on computational and applied mathematics* 20 (2017) 237–282.
- [24] S. Riffaud, M. A. Fernández, D. Lombardi, A low-rank solver for parameter estimation and uncertainty quantification in time-dependent systems of partial differential equations, *Journal of Scientific Computing* 99 (2) (2024) 34.
- [25] V. Chabannes, G. Pena, C. Prud’Homme, High-order fluid–structure interaction in 2D and 3D application to blood flow in arteries, *Journal of Computational and Applied Mathematics* 246 (2013) 1–9.
- [26] S. Deparis, D. Forti, G. Grandperrin, A. Quarteroni, FaCSI: A block parallel preconditioner for fluid–structure interaction in hemodynamics, *Journal of Computational Physics* 327 (2016) 700–718.
- [27] C. Wood, A. Gil, O. Hassan, J. Bonet, Partitioned block-Gauss–Seidel coupling for dynamic fluid–structure interaction, *Computers & structures* 88 (23-24) (2010) 1367–1382.

- [28] J. G. V. Vázquez, Nonlinear analysis of orthotropic membrane and shell structures including fluid-structure interaction., Ph.D. thesis, Universitat Politècnica de Catalunya (UPC) (2007).
- [29] J.-F. Cori, S. Etienne, A. Garon, D. Pelletier, High-order implicit Runge–Kutta time integrators for fluid-structure interactions, *International Journal for Numerical Methods in Fluids* 78 (7) (2015) 385–412. doi:10.1002/flid.4020.
- [30] S. Etienne, A. Garon, D. Pelletier, Geometric conservation law and finite element methods for 3D unsteady simulations of incompressible flow, in: 39th AIAA Fluid Dynamics Conference, 2009, p. 3571.
- [31] S. Étienne, A. Garon, D. Pelletier, Perspective on the geometric conservation law and finite element methods for ALE simulations of incompressible flow, *Journal of Computational Physics* 228 (7) (2009) 2313–2333. doi:10.1016/j.jcp.2008.11.032.
- [32] H. Bijl, M. H. Carpenter, V. N. Vatsa, C. A. Kennedy, Implicit time integration schemes for the unsteady compressible Navier–Stokes equations: laminar flow, *Journal of Computational Physics* 179 (1) (2002) 313–329.
- [33] A. van Zuijlen, H. Bijl, A higher-order time integration algorithm for the simulation of nonlinear fluid–structure interaction, *Nonlinear Analysis: Theory, Methods & Applications* 63 (5-7) (2005) e1597–e1605.
- [34] Z. Yang, D. J. Mavriplis, Higher-order time integration schemes for aeroelastic applications on unstructured meshes, *AIAA journal* 45 (1) (2007) 138–150.
- [35] S. Averweg, A. Schwarz, C. Schwarz, J. Schröder, A monolithic fluid–structure interaction approach using mixed LSFEM with high-order time integration, *Computer Methods in Applied Mechanics and Engineering* 423 (2024) 116783.
- [36] E. Hairer, G. Wanner, *Solving ordinary differential equations II: Stiff and Differential-Algebraic Problems*, Springer-Verlag Berlin Heidelberg GmbH, 1991.
- [37] R. Abu-Labdeh, S. MacLachlan, P. E. Farrell, Monolithic multigrid for implicit Runge–Kutta discretizations of incompressible fluid flow, *Journal of Computational Physics* 478 (2023) 111961.
- [38] E. Hairer, C. Lubich, G. Wanner, *Geometric Numerical Integration: Structure-Preserving Algorithms for Ordinary Differential Equations*, Springer, 2006.
- [39] A. Hay, K. Yu, S. Etienne, A. Garon, D. Pelletier, High-order temporal accuracy for 3D finite-element ALE flow simulations, *Computers & Fluids* 100 (2014) 204–217.
- [40] J. L. Eftang, A. T. Patera, Port reduction in parametrized component static condensation: approximation and a posteriori error estimation, *International Journal for Numerical Methods in Engineering* 96 (5) (2013) 269–302.
- [41] J. Ballani, D. P. Huynh, D. J. Knezevic, L. Nguyen, A. T. Patera, A component-based hybrid reduced basis/finite element method for solid mechanics with local nonlinearities, *Computer Methods in Applied Mechanics and Engineering* 329 (2018) 498–531.
- [42] M. Ebrahimi, M. Yano, A hyperreduced reduced basis element method for reduced-order modeling of component-based nonlinear systems, *Computer Methods in Applied Mechanics and Engineering* 431 (2024) 117254.
- [43] R. R. Craig Jr, M. C. Bampton, Coupling of substructures for dynamic analyses., *AIAA journal* 6 (7) (1968) 1313–1319.
- [44] P. Seshu, Substructuring and component mode synthesis, *Shock and Vibration* 4 (3) (1997) 199–210.
- [45] M. P. Castanier, Y.-C. Tan, C. Pierre, Characteristic constraint modes for component mode synthesis, *AIAA journal* 39 (6) (2001) 1182–1187.
- [46] M. Magalhaes, N. Ferguson, The development of a component mode synthesis (CMS) model for three-dimensional fluid–structure interaction, *The Journal of the Acoustical Society of America* 118 (6) (2005) 3679–3690.
- [47] Y. Yao, X. Huang, X. Yang, L. Jézéquel, Symmetric formulations combined with component mode synthesis for analyzing coupled fluid-structure problems. reviews and extensions, *Applied Mathematical Modelling* 115 (2023) 645–660.

- [48] T. Taddei, X. Xu, L. Zhang, A non-overlapping optimization-based domain decomposition approach to component-based model reduction of incompressible flows, *Journal of Computational Physics* 509 (2024) 113038.
- [49] T. Taddei, X. Xu, L. Zhang, Optimization-based model order reduction of fluid-structure interaction problems, *Journal of Computational Physics* 536 (2025) 114084.
- [50] I. Prusak, M. Nonino, D. Torlo, F. Ballarin, G. Rozza, An optimisation-based domain-decomposition reduced order model for the incompressible Navier-Stokes equations, *Computers & Mathematics with Applications* 151 (2023) 172–189.
- [51] I. Prusak, D. Torlo, M. Nonino, G. Rozza, An optimisation-based domain-decomposition reduced order model for parameter-dependent non-stationary fluid dynamics problems, *Computers & Mathematics with Applications* 166 (2024) 253–268.
- [52] M. D. Gunzburger, H. K. Lee, An optimization-based domain decomposition method for the Navier-Stokes equations, *SIAM Journal on Numerical Analysis* 37 (5) (2000) 1455–1480. doi:10.1137/S0036142998332864.
- [53] M. D. Gunzburger, J. S. Peterson, H. Kwon, An optimization based domain decomposition method for partial differential equations, *Computers & Mathematics with Applications* 37 (10) (1999) 77–93. doi:10.1016/S0898-1221(99)00127-3.
- [54] P. Kuberry, H. Lee, A decoupling algorithm for fluid-structure interaction problems based on optimization, *Computer Methods in Applied Mechanics and Engineering* 267 (2013) 594–605. doi:10.1016/j.cma.2013.10.006.
- [55] P. Kuberry, H. Lee, Analysis of a fluid-structure interaction problem recast in an optimal control setting, *SIAM Journal on Numerical Analysis* 53 (3) (2015) 1464–1487. doi:10.1137/140958220.
- [56] P. Kuberry, H. Lee, Convergence of a fluid-structure interaction problem decoupled by a Neumann control over a single time step, *Journal of Mathematical Analysis and Applications* 437 (1) (2016) 645–667. doi:10.1016/j.jmaa.2016.01.022.
- [57] L. Formaggia, A. Quarteroni, A. Veneziani, *Cardiovascular Mathematics: Modeling and simulation of the circulatory system*, Vol. 1, Springer Science & Business Media, 2010.
- [58] A. T. Barker, X.-C. Cai, Scalable parallel methods for monolithic coupling in fluid-structure interaction with application to blood flow modeling, *Journal of Computational Physics* 229 (3) (2010) 642–659. doi:10.1016/j.jcp.2009.10.001.
- [59] Y. Wu, X.-C. Cai, A fully implicit domain decomposition based ALE framework for three-dimensional fluid-structure interaction with application in blood flow computation, *Journal of Computational Physics* 258 (2014) 524–537. doi:10.1016/j.jcp.2013.10.046.
- [60] A. Shamanskiy, B. Simeon, Mesh moving techniques in fluid-structure interaction: robustness, accumulated distortion and computational efficiency, *Computational Mechanics* 67 (2) (2021) 583–600. doi:10.1007/s00466-020-01950-x.
- [61] T. Wick, Fluid-structure interactions using different mesh motion techniques, *Computers & Structures* 89 (13–14) (2011) 1456–1467. doi:10.1016/j.compstruc.2011.02.019.
- [62] F. Nobile, Numerical approximation of fluid-structure interaction problems with application to haemodynamics, Ph.D. thesis, EPFL (2001).
- [63] L. Sirovich, Turbulence and the dynamics of coherent structures. I. Coherent structures, *Quarterly of applied mathematics* 45 (3) (1987) 561–571.
- [64] S. Volkwein, Model reduction using proper orthogonal decomposition, *Lecture Notes*, Institute of Mathematics and Scientific Computing, University of Graz. see <https://www.math.uni-konstanz.de/numerik/personen/volkwein/teaching/POD-Vorlesung.pdf> (2011).
- [65] G. Rozza, K. Veroy, On the stability of the reduced basis method for Stokes equations in parametrized domains, *Computer methods in applied mechanics and engineering* 196 (7) (2007) 1244–1260.
- [66] S. Turek, J. Hron, Proposal for numerical benchmarking of fluid-structure interaction between an elastic object and laminar incompressible flow, in: *Lecture Notes in Computational Science and Engineering*, Vol. 53, Springer Berlin Heidelberg, 2006, pp. 371–385. doi:10.1007/3-540-34596-5_15.

- [67] B. Sanderse, Energy-conserving Runge–Kutta methods for the incompressible Navier–Stokes equations, *Journal of Computational Physics* 233 (2013) 100–131.